Ore Geology Reviews 165 (2024) 105880

Contents lists available at ScienceDirect

Ore Geology Reviews

journal homepage: www.elsevier.com/locate/oregeorev

Genesis of the Wutuogou Ag-Pb-Zn deposit in the Eastern Kunlun Orogenic Belt, NW China: Constraints from calcite U-Pb geochronology, mineral chemistry, and in-situ sulfur isotopes

Shuang Wang [a], Weiwei Li [a], Xu Zhao [b,c,*], Jan Marten Huizenga [d,e], Xinming Zhang [a], Chongwen Xu [a], Siqi Yu [a], Yanjun Li [a], Junhao Wei [a,*]

[a] School of Earth Resources, China University of Geosciences, Wuhan 430074, China
[b] School of Earth Science, Yunnan University, Kunming 650500, China
[c] CAS Key Laboratory of Mineralogy and Metallogeny/Guangdong Provincial Key Laboratory of Mineral Physics and Materials, Guangzhou Institute of Geochemistry, Chinese Academy of Sciences, Guangzhou 510640, China
[d] Faculty of Environmental Sciences and Natural Resource Management, Norwegian University of Life Science, Postbox 503, NO-1432 Ås, Norway
[e] Economic Geology Research Institute (EGRU), College of Science and Engineering, James Cook University, Townsville, QLD 4811, Australia

ARTICLE INFO

Keywords:
Calcite U-Pb age
Mineral chemistry
In-situ sulfur isotopes
Vein-type Ag-Pb-Zn deposit
Eastern Kunlun Orogenic Belt

ABSTRACT

The Wutuogou Ag-Pb-Zn deposit, a newly discovered vein-type deposit, is located in the Eastern Kunlun Orogenic Belt (EKOB), northwestern China. The vein-type Ag-Pb-Zn ore bodies are hosted in Middle Triassic granodiorite and monzogranite and are characterized by high-grade Ag, Pb, and Zn (average Ag: 293 g/t, Pb: 3.00 %, Zn: 2.85 %). Three paragenetic stages have been recognized: quartz + pyrite (Py-1) + arsenopyrite (stage I), pyrite (Py-2) + sphalerite + chalcopyrite + tetrahedrite + quartz (substage II-1), galena + pyrargyrite + freibergite + freieslebenite + quartz + calcite (substage II-2), and quartz + calcite (stage III). Except for Ag-bearing minerals (pyrargyrite, freibergite, and freieslebenite), invisible silver is also present in pyrite (1.91–165 ppm), sphalerite (3.86–8806 ppm), and galena (up to 0.21 wt%). The calcite is closely associated with sulfides in substage II-2 and yields a U-Pb age of 210 ± 7 Ma (MSWD = 2.7), which represents the ore-forming age (lower limit). Py-1 displays higher As contents and lower Co contents than those of Py-2, indicating a decrease in temperature from stage I to stage II. In addition, the Fe/Zn mass ratios (0.025–0.075) of sphalerite estimate the fluid temperature for substage II-1 of 246–284 °C, whereas the Ag/(Ag + Cu) and Zn/(Zn + Fe) mole ratios of freibergite estimate the fluid temperature for substage II-2 of 140–270 °C, further indicating the decrease of temperature from stage I through substage II-1 to substage II-2. Mineral assemblages of pyrite-chalcopyrite-tetrahedrite in substage II-1 and Ag-sulfosalts in substage II-2 suggest a decrease in sulfur fugacity (fS_2). Both the decrease in fS_2 and cooling of the mineralizing fluids facilitate silver precipitation. The heterogeneous compositions of the freibergite and the Ag zonation in sphalerite (Sp-1) resulted from retrograde solid-state reactions that redistributed Ag through microscale exsolution. The $\delta^{34}S$ values (+5.49 to +7.78 ‰) of the sulfides and the low Zn/Cd ratios (107–195) of sphalerite indicate a felsic magma source for the ore-forming materials. Therefore, we concluded that the Wutuogou Ag-Pb-Zn deposit corresponds to a medium- to low-temperature magmatic-hydrothermal deposit associated with Late Triassic magmatism in the Eastern Kunlun Orogenic Belt (EKOB).

1. Introduction

Hydrothermal vein-type Ag-Pb-Zn deposits are known as significant global sources of silver and base metals with high grades and abundant ore-forming elements (Baumgartner et al., 2008; Lawley et al., 2010; Mango et al., 2014; Mehrabi et al., 2016; Zhai et al., 2019; Zhai et al., 2020; Li et al., 2020a). In general, Ag-Pb-Zn ore veins are formed through open-space infill. These deposits may contain silver as the main

* Corresponding authors at: CAS Key Laboratory of Mineralogy and Metallogeny/Guangdong Provincial Key Laboratory of Mineral Physics and Materials, Guangzhou Institute of Geochemistry, Chinese Academy of Sciences, Guangzhou 510640, Guangdong Province, China (X. Zhao). School of Earth Resources, China University of Geosciences, Wuhan 430074, Hubei Province, China (J. Wei).
E-mail addresses: zhaoxu@gig.ac.cn (X. Zhao), junhaow@163.com (J. Wei).

https://doi.org/10.1016/j.oregeorev.2024.105880
Received 30 July 2023; Received in revised form 31 December 2023; Accepted 6 January 2024
Available online 9 January 2024

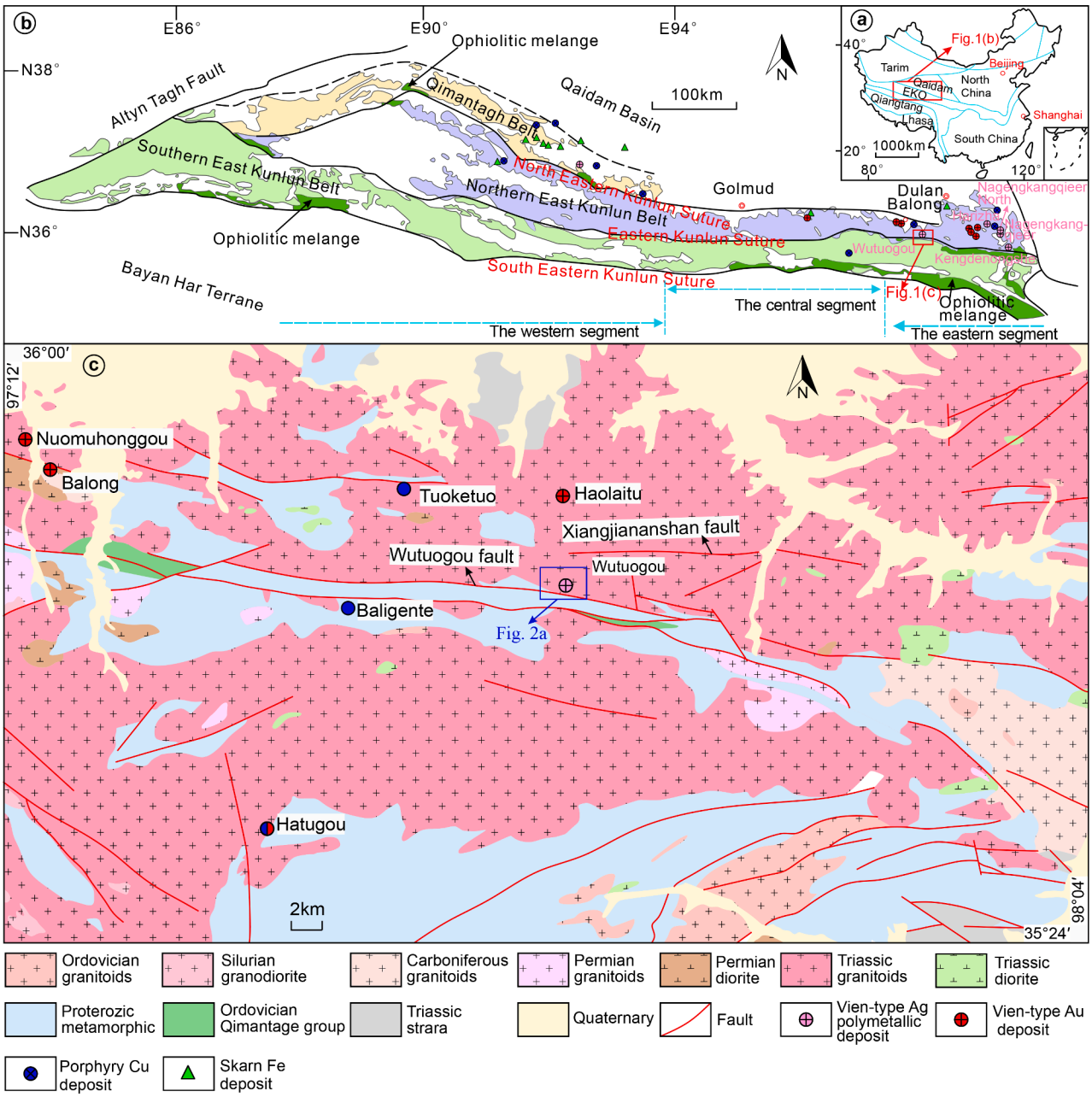

Fig. 1. (a) Tectonic map of China showing the location of the EKOB, after (Yuan et al., 2010). (b) Structural sketch of the EKOB showing the location of study area, after (Dong et al., 2018). (c) Geology of the Wutuogou Ag-Pb-Zn deposit and surrounding areas.

commodity or as a co-existing product with lead and zinc ores (Zhai et al., 2020). Silver is often associated with sulfides and predominantly occurs as Ag-bearing sulfosalts (Mango et al., 2014; Li et al., 2019; Zhai et al., 2019; Qi et al., 2022; Zhang et al., 2023a). Previous studies have primarily concentrated on investigating the distribution of silver in pyrite or sphalerite (Li et al., 2016; Yu et al., 2020a; Wang et al., 2022; Zhang et al., 2022), leaving a need for comprehensive research on the distribution of silver within common sulfides and Ag-bearing sulfosalts in specific vein-type Ag-Pb-Zn deposits. Some researchers suggest that the precipitation of silver from hydrothermal fluids is primarily controlled by decreases in temperature, pH, fO_2, and fS_2 (Li et al., 2019; Zhai et al., 2019; Zhang et al., 2023a); others argue that it is influenced by fluid mixing and dilution (Baumgartner et al., 2008; Li et al., 2016). However, further study is still required to better understand the formation conditions for hydrothermal vein-type Ag-Pb-Zn deposits. In some cases, Ag-Pb-Zn veins are frequently found in association with magmatic-hydrothermal systems (Lawley et al., 2010; Box et al., 2012; Catchpole et al., 2015; Zhai et al., 2019; Li et al., 2020a; Zhang et al., 2023a). Nevertheless, certain deposits of this type do not seem to have a clear genetic connection to magmatic activity (Beaudoin and Sangster, 1992; Kissin and Mango, 2014). The origin of their ore-forming materials remains a subject of debate.

Reliable ore-forming ages are vital for comprehending regional large-scale mineralization as well as the genetic relationship between mineralization and magmatism of this type deposit (Zhai et al., 1999; Mederer et al., 2014; Yan et al., 2021). Nevertheless, it is still difficult to constrain the ore-forming age of hydrothermal Ag-Pb-Zn ore veins. At present, Rb-Sr and Re-Os dating of sulfides, U-Th-Pb dating of U-bearing hydrothermal auxiliary minerals, and $^{40}Ar/^{39}Ar$ and Rb-Sr dating of K-bearing alteration minerals are commonly used to constrain the mineralization age of hydrothermal vein-type deposits (Selby et al., 2002; Baumgartner et al., 2008; Li et al., 2012; Catchpole et al., 2015).

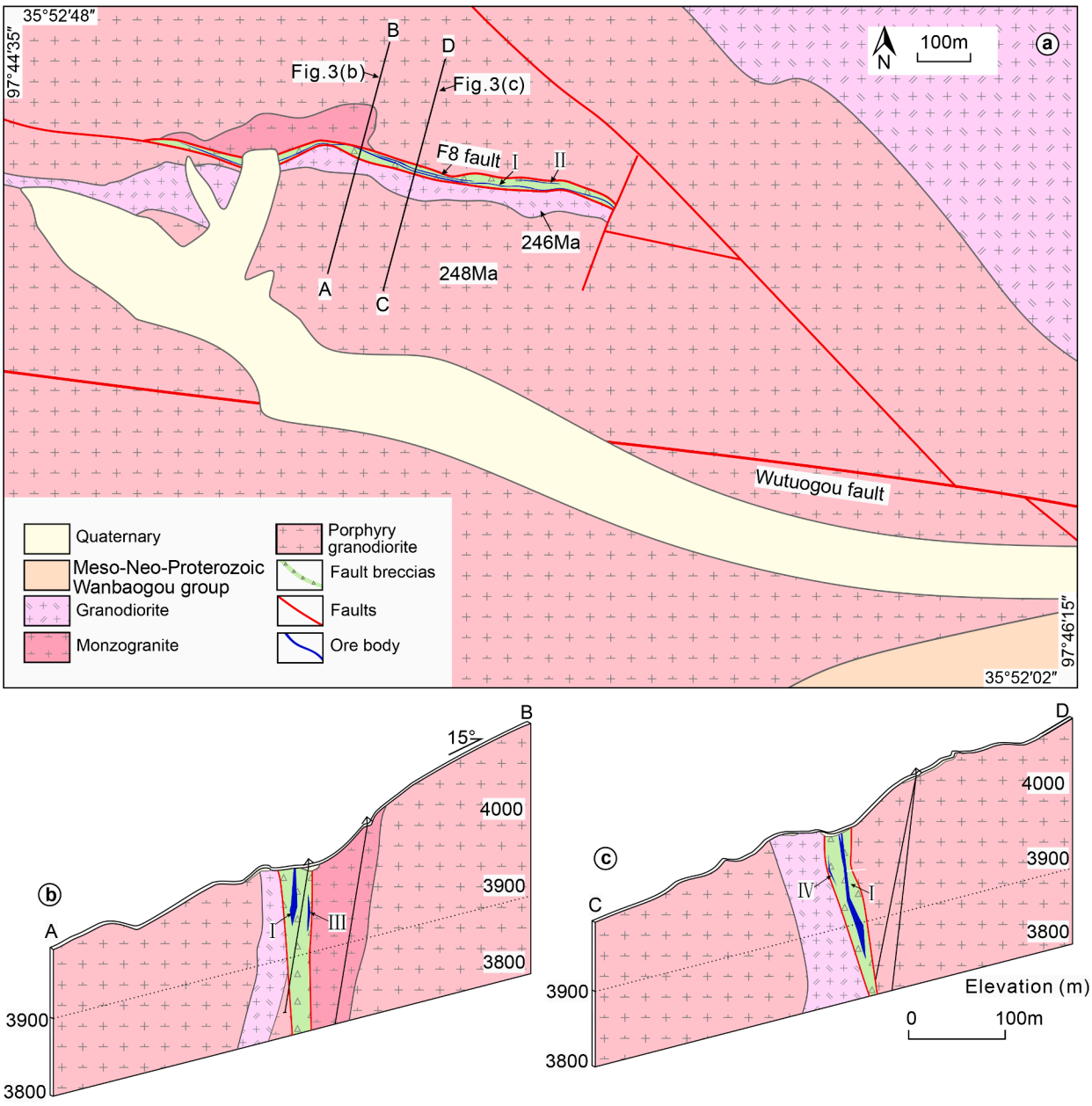

Fig. 2. (a) Geological map of the Wutuogou Ag-Pb-Zn deposit. (b and c) Representative cross sections along exploration lines 03 (A and B) and 02 (C and D) show the occurrence and morphology of the major orebodies at the Wutuogou Ag-Pb-Zn deposit. The locations of the sections are shown in Fig. 2a. The ages of granodiorite and monzogranite are from Li et al. (2018).

However, it is challenging to precisely establish the Re-Os isotopic composition of the samples with currently available instrumental sensitivity because most of the sulfides associated with vein-type Ag-Pb-Zn deposits have low Re contents. The degree of homogeneity in the initial isotopic composition and the level of fractionation in the parent or daughter isotopes have a significant impact on the Rb-Sr isochron method. In addition, the absence of auxiliary minerals containing U in some vein-type Ag-Pb-Zn deposits prevents the use of the U-Th-Pb method for auxiliary minerals. In recent years, the laser ablation-inductively coupled plasma-mass spectrometry (LA-ICP-MS) U-Pb dating method has been developed for calcite with a low U content, offering an alternative dating method for hydrothermal deposits (Coogan et al., 2016; Burisch et al., 2018; Drake et al., 2020; Jin et al., 2021). The calcite is usually associated with sulfides in the vein-type Ag-Pb-Zn deposit, providing us with studied objects to determine the ore-forming age.

The Eastern Kunlun Orogenic Belt (EKOB) records the complex evolution history of the Paleo-Tethys. This occurred during the late Paleozoic to early Mesozoic, resulting in the generation of extensive magmatic rocks and numerous metal deposits containing abundant Au, Cu, Ag, Pb, Zn, and Fe (Xu et al., 2006; Yu et al., 2017; Chen et al., 2020a; Zhao et al., 2021; Zhang et al., 2023b). In recent years, many Ag polymetallic deposits have been discovered in the eastern segment of the EKOB, including the Nagengkangqieer Ag deposit, the Nagengkangqieer North Ag deposit, the Gemalong Ag polymetallic deposit, the Harizha Ag polymetallic deposit, the Kengdenongshe Au-Ag-Pb-Zn deposit, and the Wutuogou Ag-Pb-Zn deposit (Zhang et al., 2018; Chen et al., 2020b; Fan et al., 2021; Zhao et al., 2021; Zhang et al., 2023a). Among these, the Wutuogou Ag-Pb-Zn deposit is distinctive as its ore bodies are hosted in granitoids, whereas the ore bodies in other deposits are hosted in Triassic volcanic or sedimentary rocks. The ore bodies in the Wutuogou Ag-Pb-Zn deposit are characterized by high grade (Ag: 293 g/t, Pb: 3.00

%, Zn: 2.85 %) and a consistent orientation of the ore bodies, which implies that there is a potential for further exploration in the region. Therefore, it is important to constrain the deposit geology, mineralization timing, and genetic type of the Wutuogou Ag-Pb-Zn deposit to understand the regional Ag-Pb-Zn metallogenic events in the EKOB.

In this study, we determined the age of the Wutuogou Ag-Pb-Zn deposit using the U-Pb dating of calcite. In addition, we conducted analyses on the geochemistry of sulfide and Ag-bearing minerals, along with in-situ sulfur isotopic compositions of sulfides. These investigations were carried out to constrain the distribution of silver, understand the physicochemical conditions of mineralization, and elucidate the genesis of the deposit.

2. Regional geology

The EKOB is bounded to the north by the Qaidam Basin and to the south by the Bayan Har Terrane. It extends from the Qinling Orogen in the east to the Altyn Tagn Fault in the west (Pan et al., 2012; Dong et al., 2022) (Fig. 1b). From south to north, the Southern Eastern Kunlun Suture, the Central Eastern Kunlun Suture, and the Northern Eastern Kunlun Suture divide the EKOB into three belts, e.g., the Southern Eastern Kunlun Belt, the Central Eastern Kunlun Belt, and the Northern Qimantagh Belt, respectively (Dong et al., 2018; Li et al., 2020b; Zhao et al., 2022a) (Fig. 1b). The Central Eastern Kunlun Suture is related to the closure of the Proto-Tethys Ocean during the Proterozoic-Early Paleozoic period. The Southern East Kunlun Fault is the result of the closure of the Paleo-Tethys Ocean in the Middle Triassic (Zhong et al., 2017; Li et al., 2020b; Fu et al., 2022; Zhang et al., 2023b). The basement rocks in the EKOB include migmatite, granulite, felsic gneiss, and amphibolite from the Paleoproterozoic Jinshuikou Group and gneiss, amphibolite, marble, and metasandstone from the Meso-Neoproterozoic Xiaomiao Formation (Huang et al., 2014; Chen et al., 2017a). The basement rocks are covered by low-grade metamorphic rocks from the Ordovician Nachitai Group and discontinuous Carboniferous to Neogene sedimentary and volcanic rocks (Chen et al., 2017b). Paleozoic-Mesozoic granitoids in the EKOB were formed at 470–390 Ma and 260–200 Ma (Huang et al., 2014; Dong et al., 2018; Chen et al., 2020a; Zhao et al., 2021; Zhang et al., 2023b) (Fig. 1c). The granitoids from both age groups are associated with subduction and closure of the Proto-Tethys Ocean and the Paleo-Tethys Ocean, respectively, and subsequent post-collisional magmatism (Zhang et al., 2014; Chen et al., 2020a; Li et al., 2020c; Zhao et al., 2022b). Mafic-ultramafic rocks are found in the vicinity of the Central East Kunlun Fault, with ages ranging from 537 to 467 Ma. They are also present in the Southern East Kunlun Fault region, with ages spanning 555 to 516 Ma and 345 to 332 Ma (Dong et al., 2018; Yu et al., 2020b).

The EKOB contains several large to medium-sized metal deposits. The western part of the EKOB hosts numerous porphyry and skarn deposits (Fang et al., 2018; Zhong et al., 2018), whereas the central segment is characterized by occurrences of vein-type gold deposits (Zhang et al., 2017; Wu et al., 2021). The eastern part of the EKOB contains different deposit types, including vein-type gold, vein-type Ag polymetallic, porphyry Cu-Mo, and skarn Fe deposits (Zhao, 2020; Chen et al., 2020b) (Fig. 1b and c). In recent years, silver mining has been one of the priorities of mineral exploration in the eastern part of the EKOB, as a series of Ag (polymetallic) deposits were discovered (i.e., the Harizha Ag polymetallic deposit, the Kengdenongshe Au-Ag-Pb-Zn polymetallic deposit, the Nagengkangqieer Ag deposit, the Gemalong Ag polymetallic deposit, and the Wutuogou Ag-Pb-Zn deposit) (Chen et al., 2020b; Fan et al., 2021; Zhao et al., 2021). The Wutuogou Ag-Pb-Zn deposit, which is the focus of this study, is hosted in granitoids, whereas the other Ag polymetallic deposits are hosted in Triassic volcanic and sedimentary rocks.

Table 1
Descriptions of the wall rocks in the Wutuogou Ag-Pb-Zn deposit.

Rock types	Cross-cutting relationship	mineralogical assemblages	Age (Ma)	Reference
Granodiorite	Cutting the Proterozoic Wanbaogou group and cut by the ore body	Quartz (20–25 %) Plagioclase (50–55 %)K-feldspar (30–35 %) Hornblende (5 %)	248	Li et al., 2018
Monzogranite	Cut by the ore body	Plagioclase (40–45 %)K-feldspar (30–35 %) Quartz (20–25 %) Hornblende (2 %) Biotite (2 %)	246	Li et al., 2018

3. Deposit geology

3.1. Geology of the Wutuogou Ag-Pb-Zn deposit

The Wutuogou Ag-Pb-Zn deposit is situated in the eastern segment of the EKOB, north of the Central East Kunlun Fault (Fig. 1c). The Ag-Pb-Zn ore bodies are hosted in the fault between granodiorite (248 Ma) and monzogranite (246 Ma) (Fig. 2a, Table 1). Previous studies have shown that both the granodiorite and monzogranite in the deposit area were formed in a continental arc setting related to the subduction of the Paleo-Tethys Ocean (Li et al., 2018). The granodiorite is covered by the Quaternary sedimentary rocks in the central part of the ore district and intruded into the Proterozoic Wanbaogou Group in the southwest (Fig. 2).

Northwest and northwest-west trending faults are common in the ore district (Fig. 2). The NWW-trending Wutuogou Fault is a segment of the Central Eastern Kunlun Suture, cutting the southern part of the ore district. The F8 fault is a second-order fault of the Wutuogou fault and controls the occurrence, shape, and size of the ore bodies. The F8 fault dips 70° to the northeast and has a length of 1 km and a width of 5–30 m (Fig. 2).

3.2. Ag-Pb-Zn mineralization

Five Ag-Pb-Zn ore bodies (I-V) were identified in the Wutuogou Ag-Pb-Zn deposit (Fig. 2), with an average Pb + Zn grade of 5.8 % and an Ag grade of 293 g/t, respectively. The five vein-type lenticular-shaped ore bodies are 1–2 m thick and dip at an angle of over 70° to the northeast (Fig. 2). The Ag-Pb-Zn mineralization occurs as massive, brecciated, and veined ores (Fig. 3), which are characterized by extensive alteration as exemplified by silicification, carbonation, and the presence of chlorite, epidote, and sericite.

Three mineralization stages were recognized based on mineral assemblage and cross-cutting relationships in the Wutuogou Ag-Pb-Zn deposit. They include a quartz-pyrite-arsenopyrite stage I, a polymetallic sulfide-silver stage II, and a calcite-quartz stage III.

Stage I is characterized by a mineral assemblage of quartz, pyrite (Py-1), and arsenopyrite (Fig. 3a and c). Euhedral Py-1 coexists with arsenopyrite and quartz and is being replaced by sphalerite, galena, pyrargyrite, and freibergite (Fig. 4a–d). The quartz-pyrite veins from this stage have been replaced by ore veins from stage II (Fig. 3a).

Stage II represents the main mineralization stage, comprising polymetallic sulfides and Ag-bearing minerals. It can be subdivided into substages II-1 and II-2 (Fig. 3g–i). Sphalerite-dominated ore veins of substage II-1 have been crosscut and replaced by galena-dominated ore veins of substage II-2 (Fig. 3g–i). Substage II-1 is represented by a

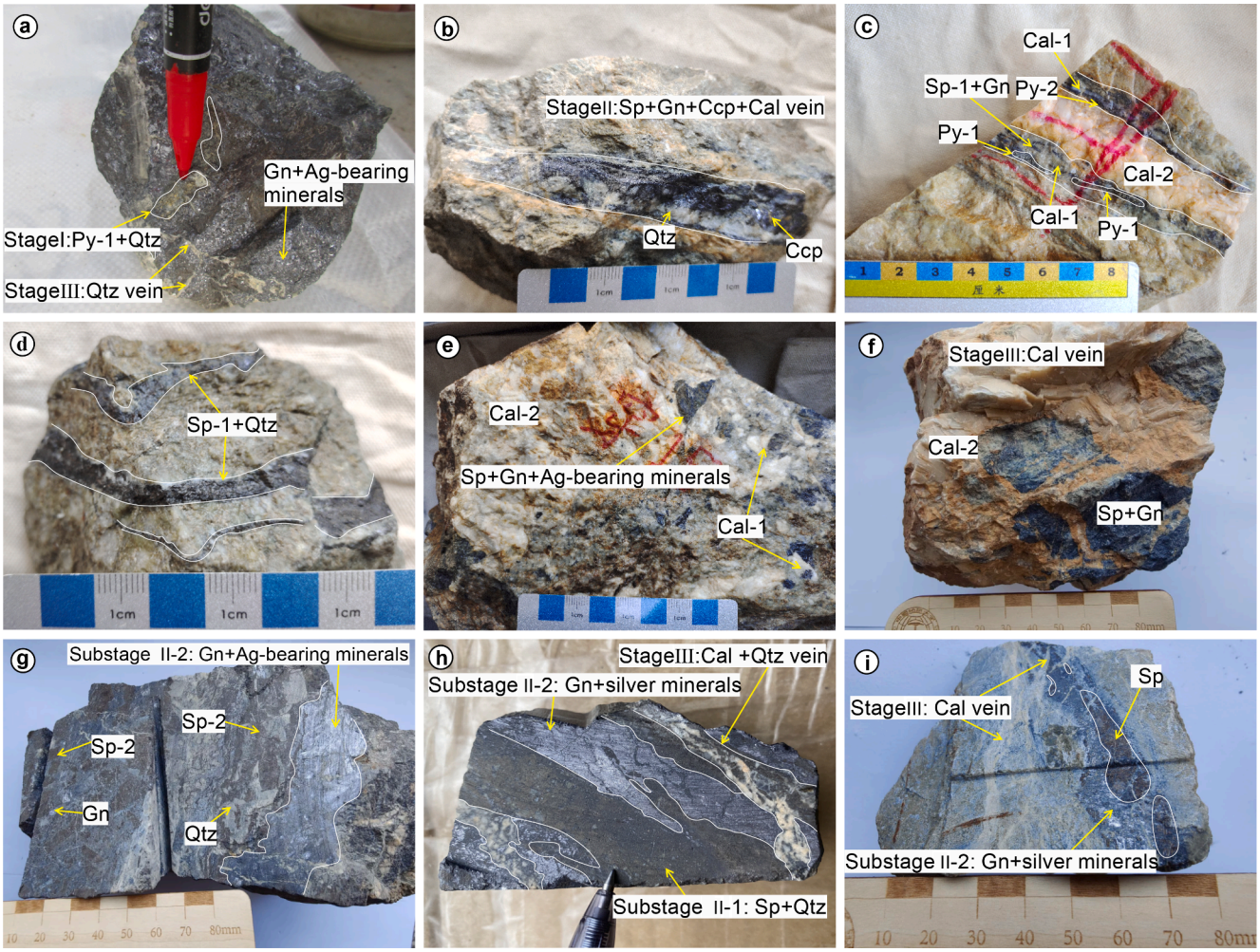

Fig. 3. Representative photographs of ores from the Wutuogou Ag-Pb-Zn deposit. (a) Galena and Ag-bearing sulfosalts replaced quartz and pyrite in Stage I. (b) Sphalerite-galena-chalcopyrite-quartz vein. (c) Late calcite crosscuts the early-formed ore veins. (d) Sphalerite-galena-quartz veins occur in wall rock, accompanied by chlorite and epidote alteration. (e) Late calcite cemented sphalerite-galena and calcite breccia. (f) Late calcite cemented ore brecciated. (g) Galena replaced early-formed brecciated sphalerite and quartz. (h) Late calcite crosscut early ores, and galena replaced sphalerite. (i) Late calcite veins crosscut the early galena and sphalerite veins. Qtz = quartz, Cal = calcite, Py = pyrite, Ccp = chalcopyrite, Sp = sphalerite, Gn = galena.

mineral assemblage comprising pyrite (Py-2), sphalerite, and quartz with minor chalcopyrite. Sulfides of this stage occur in veined and brecciaed ores (Fig. 3d and g).

Substage II-2 is characterized by quartz, calcite (Cal-1), galena, and Ag-bearing minerals with minor chalcopyrite, tetrahedrite, and smithsonite. These sulfides and Ag-bearing minerals occur in massive, veined, and brecciated ores (Fig. 3a, b, e). Galena replaces pyrite, sphalerite, and freibergite (Fig. 4d–g), all of which are replaced by pyrargyrite (Fig. 4b and k). Ag-bearing minerals, such as pyrargyrite, freibergite, freieslebenite, and native silver, exist as irregular grains or veinlets within sphalerite, galena, pyrite, and quartz, or as exsolution inclusions within galena (Fig. 4h–l, Fig. S1c and f). Cal-1 occurs in veined and brecciaed ores, associated with sphalerite and galena (Fig. 3c and e).

Stage III signifies the end of mineralization. This stage is dominated by quartz and calcite (Cal-2), in which Cal-2 occurs as open-space fillings that cement the breccia or crosscut ore veins (Fig. 3f and i, Fig. S1g and h). The mineral assemblages and paragenetic sequences described above are summarized in Fig. S2.

4. Sampling and analytical methods

Samples were collected from underground tunnels, and detailed information about each sample is summarized in Table 2. Petrographic analysis was carried out on polished thin sections of samples to determine the mineral composition, textures, and paragenesis. The samples were analyzed by backscattered electron (BSE), electron probe microanalyzer analysis (EPMA), and laser ablation-inductively coupled plasma-mass spectrometry (LA-ICP-MS).

4.1. LA-ICP-MS U-Pb dating of calcite

Calcite U-Pb isotopic analysis was done using laser ablation-inductively coupled plasma-mass spectrometry (LA-ICP-MS) at the Micro-Origin and Spectrum Laboratory, Sichuan Chuangyuan Weipu Analytical Technology Co. Ltd. Cathodoluminescence (CL) imaging was used to examine the calcite texture. Following the standard methods described by Nuriel et al. (2021), Roberts et al. (2017), and Luo et al. (2020), laser sampling was performed using an ASI Resolution LR 193 nm ArF excimer laser ablation (LA) system, and ion-signal intensities were acquired using a Thermo Fisher iCAP-TQ ICP-MS instrument. The laser timing was set at three seconds for surface cleaning, seven seconds for washout, 15 s for background, and 20 s for ablation. Calcite was ablated at a spot size of 120 μm using 15 Hz repetition rate and a 3.0 J/cm^2 fluence. The NIST 614 glass was utilized as a primary reference material to bracket carbonate reference materials and the samples at every five intervals for the correction of the $^{207}Pb/^{206}Pb$ ratios of the

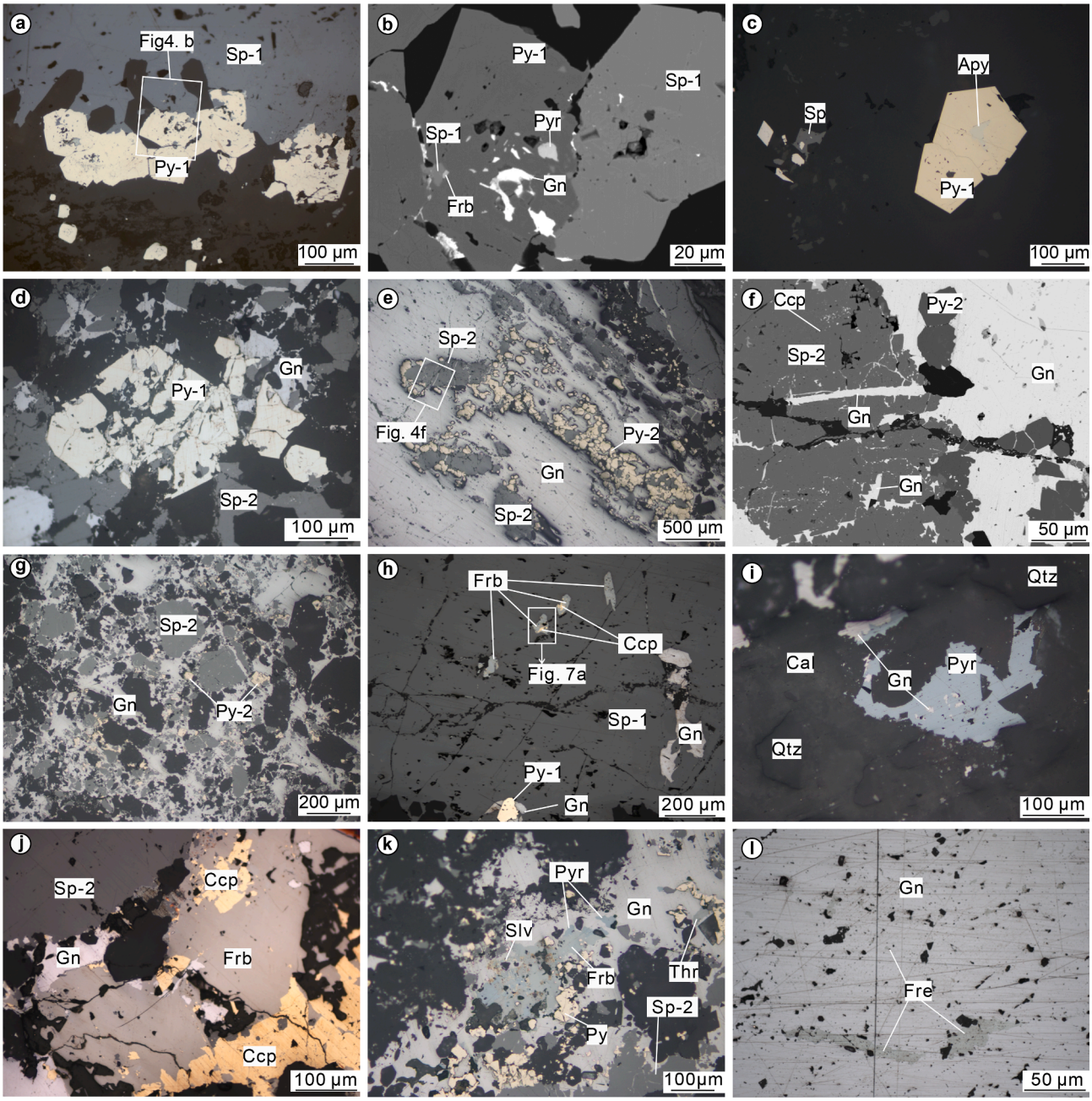

Fig. 4. Photomicrographs showing mineral assemblages and textures of ores from the Wutuogou Ag-Pb-Zn deposit. Figures b and f are BSE images, and other photographs are reflected light images. (a) Sphalerite replaces early pyrite and quartz. (b) Irregular sphalerite, galena, pyrargyrite, and freibergite replace pyrite. (c) Arsenopyrite is enveloped by pyrite. (d) Sphalerite replaces pyrite, and pyrite and sphalerite are replaced by galena. (e) Galena replaces pyrite and sphalerite. (f) Sphalerite with 'chalcopyrite disease' is replaced by galena crosscutting veinlets. (g) Early-formed sphalerite and pyrite are surrounded by galena. (h) Freibergite, coexisting with chalcopyrite, is surrounded by sphalerite. (i) Pyrargyrite occurs as an irregular grain in quartz and replaces galena. (j) Freibergite is intergrown with galena and chalcopyrite, and sphalerite is replaced by galena and freibergite. (k) Pyrargyrite is intergrown with silver and replaces freibergite, pyrite, galena, and sphalerite. (l) Freieslebenite is intergrown with galena. Qtz = quartz, Cal = calcite, Py = pyrite, Ccp = chalcopyrite, Sp = sphalerite, Gn = galena, Apy = arsenopyrite, Pyr = pyrargyrite, Frb = freibergite, Fre = freieslebenite, Thr = tetrahedrite.

reference material and samples (Woodhead et al., 2001). The $^{238}U/^{206}Pb$ ratios of the calcite samples were subsequently calibrated with in-house standards (AHX-1d, 238.2 ± 0.9 Ma) and cross-checked with ID-MS calibrated calcite standard (PTKD-2, 153.7 ± 1.7 Ma) and an internal intensive LA calibrated standard (LD-5, 72.5 ± 1.0 Ma) for age reliability and accuracy (Kendrick et al., 2022). Our measurements gave lower intercept ages of 238.3 ± 1.7 Ma (MSWD = 3.0, n = 25) for AHX-1d, 154.7 ± 2.2 Ma (MSWD = 1.1, n = 24) for PTKD-2, and 73.5 ± 0.6 Ma (MSWD = 1.4, n = 26) for LD-5. These ages are indistinguishable from the standard values for AHX-1d, PTKD-2, and LD-5, respectively. Experimental data processing was done using Iolite 4 (Paton et al., 2011), and concordia diagrams were constructed using Isoplot 3 (Ludwig, 2003).

4.2. SEM, EDS analysis and EPMA

Backscattered electron (BSE) images, energy dispersive X-ray spectroscopy analysis, and wavelength dispersive electron probe microanalyzer analysis (EPMA) were performed at the Wuhan Sample Solution Analytical Technology Co., Ltd., Wuhan, China. BSE images

Table 2
Descriptions of samples used for this study.

Sample No.	Stage	Ore structure	Ore minerals		Gangue minerals	Cross-Section	Analyses
			Major	Minor			
67	II-1, II-2	veined	Sp, Gn	Py, Apy, Ccp, Pyr	Qtz, Cal	3990 m	BSE, LA-ICP-MS, EPMA
69	I, II-1	veined	Sp, Py	Gn, Ccp, Frb, Pyr	Qtz	3990 m	BSE, LA-ICP-MS, EPMA
71	II-1, II-2	brecciated	Gn, Sp	Ccp, Frb, Pyr	Qtz, Cal	3990 m	BSE, EPMA
74	II-1, II-2	veined	Gn, Sp	Ccp, Frb, Pyr, Fre	Qtz, Cal	3990 m	BSE, EPMA
76	II-1, II-2	brecciated	Gn, Sp	Frb, Pyr, Fre	Qtz, Cal	3930 m	BSE, EPMA
78	I, II-1	massive	Gn, Sp, Py	Py, Pyr	Qtz	3930 m	BSE, LA-ICP-MS, EPMA
82	II-1, II-2	brecciated	Sp, Gn, Py	Ccp, Frb, Pyr, Fre, Thr	Qtz, Cal	3930 m	BSE, LA-ICP-MS, EPMA
84	II-1, II-2	brecciated	Sp, Gn	Py, Ccp, Frb, Pyr, Fre,	Qtz	3930 m	BSE, EPMA
88	II-1, II-2	brecciated	Gn, Sp	Frb, Pyr	Qtz, Cal	3930 m	Calcite U-Pb, CL

Qtz = quartz, Cal = calcite, Py = pyrite, Ccp = chalcopyrite, Sp = sphalerite, Gn = galena, Apy = arsenopyrite, Pyr = pyrargyrite, Frb = freibergite, Fre = freieslebenite, Thr = tetrahedrite.

were acquired using a Zeiss Supra 55 field emission scanning electron microscope (SEM, JSM-IT100, Japan Electron Optics Laboratory Co., Ltd., Tokyo, Japan), with an accelerating voltage of 15 kV, a primary beam current of 20 nA, and an image acquisition time of 35 s/sheet. A JEOL EX-230 was utilized for the EDS analysis using an accelerating voltage of 20 kV and a beam current of 40–80 nA. A JEOL JXA-8230 electron probe microanalyzer was used for major element analyses of pyrite, sphalerite, galena, pyrargyrite, freibergite, and freieslebenite using carbon-coated polished thin sections. The sulfides were analyzed at a 20 kV accelerating voltage and a 20 nA beam current with a 1 μm spot diameter. A 5 μm spot diameter, a 20 kV accelerating voltage, and a 5 nA beam current were used to analyze the Ag-bearing minerals. Peak and background analysis were done for 20 and 10 s, respectively. All data were corrected using the standard ZAF correction method from JEOL. The standards that were used include arsenopyrite, pyrite, sphalerite, chalcopyrite, galena, pentlandite, native gold, native silver, native cobalt, native germanium, native cadmium, and native bismuth.

4.3. LA-ICP-MS trace elemental analysis of sulfides

The trace element contents of the sulfides were determined using laser ablation-inductively coupled plasma-mass spectrometry (LA-ICP-MS) at the Wuhan Sample Solution Analytical Technology Co., Ltd., Wuhan, China. The laser ablation system and the ICP-MS instrument operating conditions are described by Zong et al. (2017). The GeolasPro laser ablation system, which comprises a MicroLas optical system and a COMPexPro 102 ArF excimer laser with a wavelength of 193 nm and a maximum energy of 200 mJ, was used to accomplish the laser sampling. Ion signal intensities were obtained using an Agilent 7700e ICP-MS instrument. This laser ablation system contains a "wire" signal smoothing device (Hu et al., 2015). Helium was used as the carrier gas. The spot size and frequency of the laser were set to 32 μm and 8 Hz, respectively.

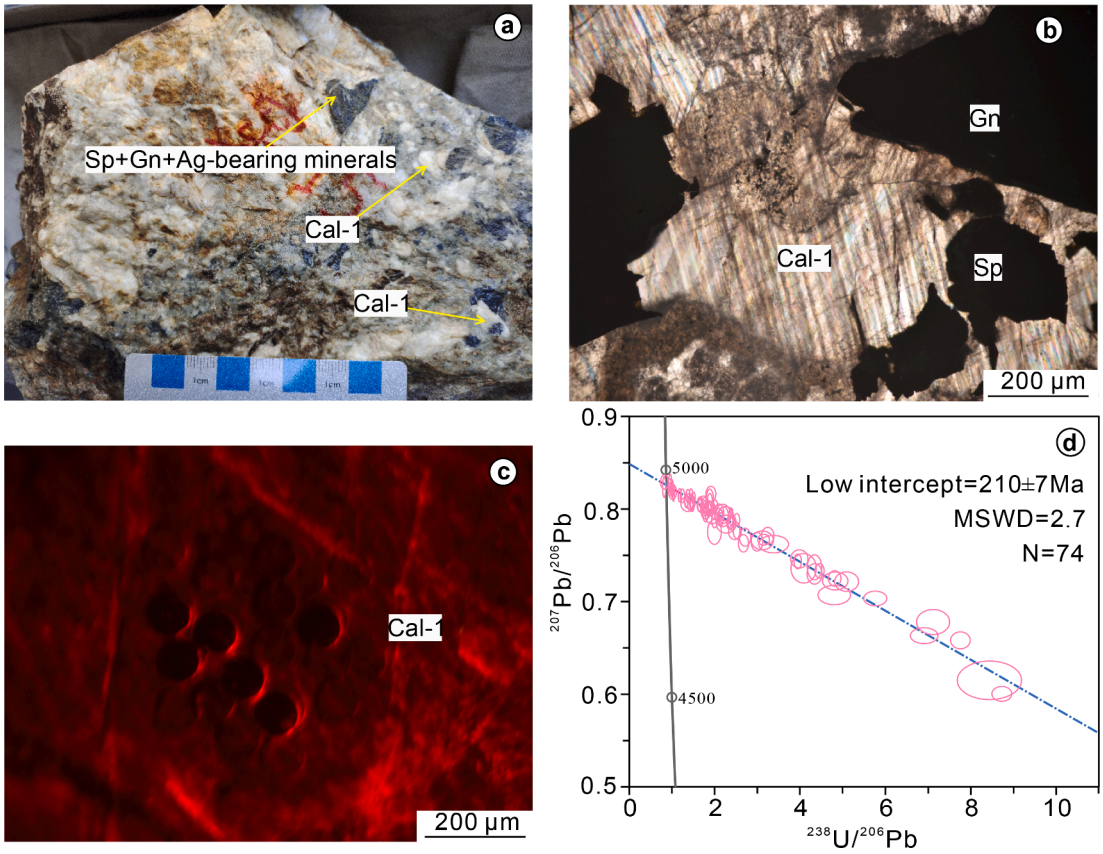

Fig. 5. (a) Late calcite cemented sphalerite, galena, and calcite breccia. (b) Reflected light images of calcite intergrown with sulfides. (c) Cathodoluminescence image of Cal-1. (d) U-Pb Terra-Wasserburg concordia diagram for calcite from the Wutuogou Ag-Pb-Zn deposit.

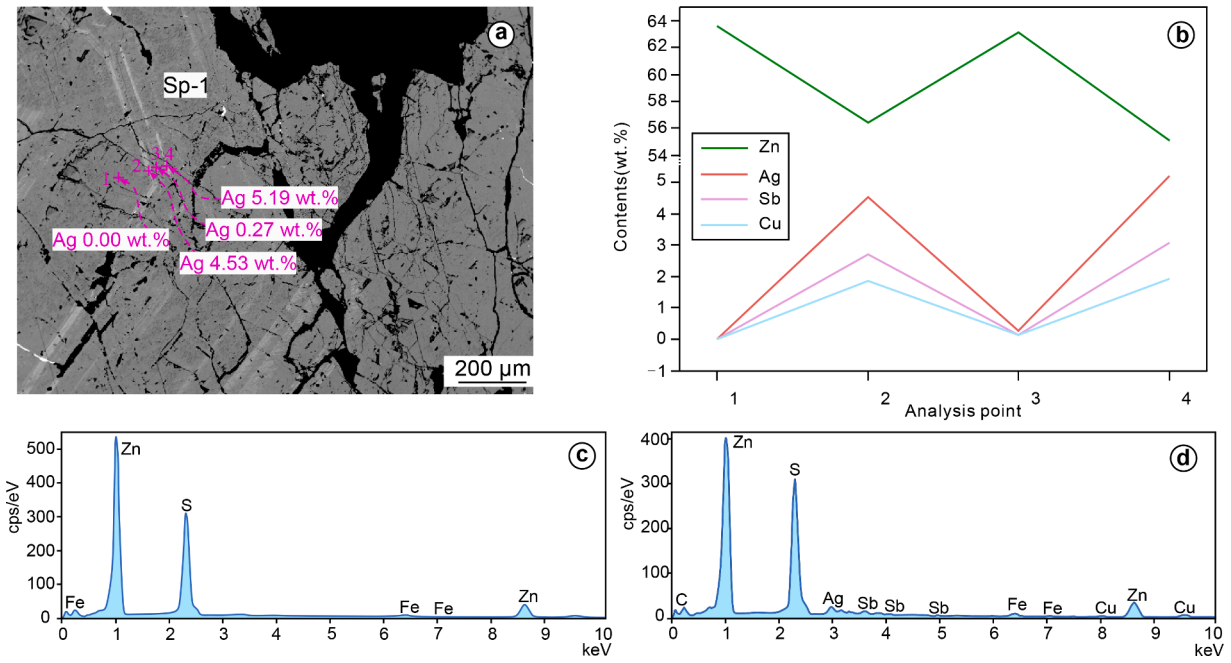

Fig. 6. (a) Sphalerite with high Ag content zoning texture (BSE image). The Ag content was determined by EPMA. (b) Ag, Sb, Cu, and Zn contents, determined by EPMA, vary in the bright and dark zones in sphalerite. The X-axis shows spot analysis from (a). (c) EDS spectra of analysis point 1 in (a). (d) EDS spectra of analysis point 2 show high Ag content in (a).

For each spot analysis, background data was collected for roughly 20–30 s before sample data was acquired for 50 s. As external standards, measurements were performed against the synthetic glass standard NIST 610 and the sulfide standard MASS-1 of the United States Geological Survey. The following elements were monitored: ^{55}Mn, ^{57}Fe, ^{59}Co, ^{60}Ni, ^{65}Cu, ^{66}Zn, ^{69}Ga, ^{72}Ge, ^{75}As, ^{77}Se, ^{95}Mo, ^{107}Ag, ^{111}Cd, ^{115}In, ^{118}Sn, ^{121}Sb, ^{125}Te, ^{195}Pt, ^{197}Au, ^{205}Tl, ^{208}Pb, and ^{209}Bi. The software Iolite 4 was used to perform off-line selection signals and quantitative calibration for trace element analysis (Paton et al., 2011). The Fe and Zn contents determined by EPMA were used as the internal standards for pyrite and sphalerite, respectively.

4.4. In-situ S isotope analysis

In-situ sulfur isotope analysis was determined using a RESOlution SE 193-nm New Wave ArF Excimer laser coupled and a multi-collector inductively coupled plasma mass spectrometer (Neptune Plus) at Beijing Createch Texting Technology Co., Ltd., Beijing, China. S isotope analyses were done using a spot diameter of 24 μm, a laser energy density of 8 J/cm^2, and a frequency of 8 Hz. The ablated materials were transferred into the plasma using high-purity He as a carrier gas. Each analysis consisted of 40 s of sample and 30 s of background data, with a Nu Plasma II integration time of 0.3 s. The Wenshan natural pyrite crystal (GBW07267, developed by the Chinese Academy of Geological Sciences, Beijing, China) was used as a standard, and the reproducibility of δ^{34}S measurements was better than 0.6 ‰. The instrumental mass discrimination was corrected using the balmat FeS, MXG, and balmat ZnS standards. All S isotope values are expressed in the delta notation in per mil (‰) relative to the Cañion Diablo Troilite (CDT) standard.

5. Results

5.1. Calcite U-Pb age

Calcite (Cal-1) from sample WT-88 is milky-white in color. They occur as breccias macroscopically and distribute around the breccias of sulfide (Fig. 5a). The early breccias of Cal-1 and sulfide are cemented by the grayish Cal-2. In CL images, Cal-1 displays a distinct red color (Fig. 5c). It is texturally intergrown with sphalerite and galena, which are associated with Ag mineralization (Fig. 5b). Therefore, the calcite U-Pb age represents the mineralization age (lower limit) of the Wutuogou Ag-Pb-Zn deposit.

The U-Pb isotopic data for calcite are tabulated in Table S1 and illustrated in the Terra-Wasserburg diagram (Fig. 5d). The calcite contains Pb (0.31–12.4 ppm) and U (0.14–2.79 ppm). The ^{238}U/^{206}Pb ratios range from 0.851 to 9.091 (average of 2.794), and the ^{207}Pb/^{206}Pb ratios vary from 0.600 to 0.829 (average of 0.777). All the analyses yielded a lower intercept age of 210 ± 7 Ma for the calcite on the Terra-Wasserburg diagram (Fig. 5d).

5.2. Mineral textures, types, and major elements

The sulfide mineral phases in the Wutuogou Ag-Pb-Zn deposit are pyrite, sphalerite, and galena. The Ag-bearing minerals are identified as pyrargyrite, freibergite, freieslebenite, and minor native silver (Fig. 4). The major element compositions and calculated chemical formulas of these sulfides and Ag-bearing minerals are presented in Table S2.

5.2.1. Sulfides

Py-1 presents in stage I and is characterized by euhedral crystals. It shows a pentagonal dodecahedron habit, with diameters ranging from 50 to 300 μm (Fig. 4a–d). Py-1 has Fe, S, and As contents of 45.95–46.63 wt%, 52.11–53.51 wt%, and 0.09–2.02 wt%, respectively. Py-2 occurs in substage II-1 and is characterized by subhedral-allotriomorphic crystals. It has a diameter of 30–100 μm, of which the rim is replaced by sphalerite and galena (Fig. 4e and f). Py-2 has a similar S content (51.44–53.75 wt%) as Py-1, a slightly lower Fe content (45.08–46.27 wt %), and a higher As content (0.56–2.52 wt%).

Two sphalerite types, Sp-1 and Sp-2, have been recognized in substage II-1. Sp-1 appears in vein and Sp-2 in breccia. Sp-1 contains minor inclusions of quartz, galena, chalcopyrite, pyrargyrite, and freibergite (Fig. 4a and h). The back-scattered electron (BSE) images of Sp-1 show a clear ring-zone texture (Fig. S1b, Fig. 6a). Sp-1 displays a wide range for the Zn (55.07–64.75 wt%), Ag (<5.19 wt%), Sb (<3.06 wt%), and Cu

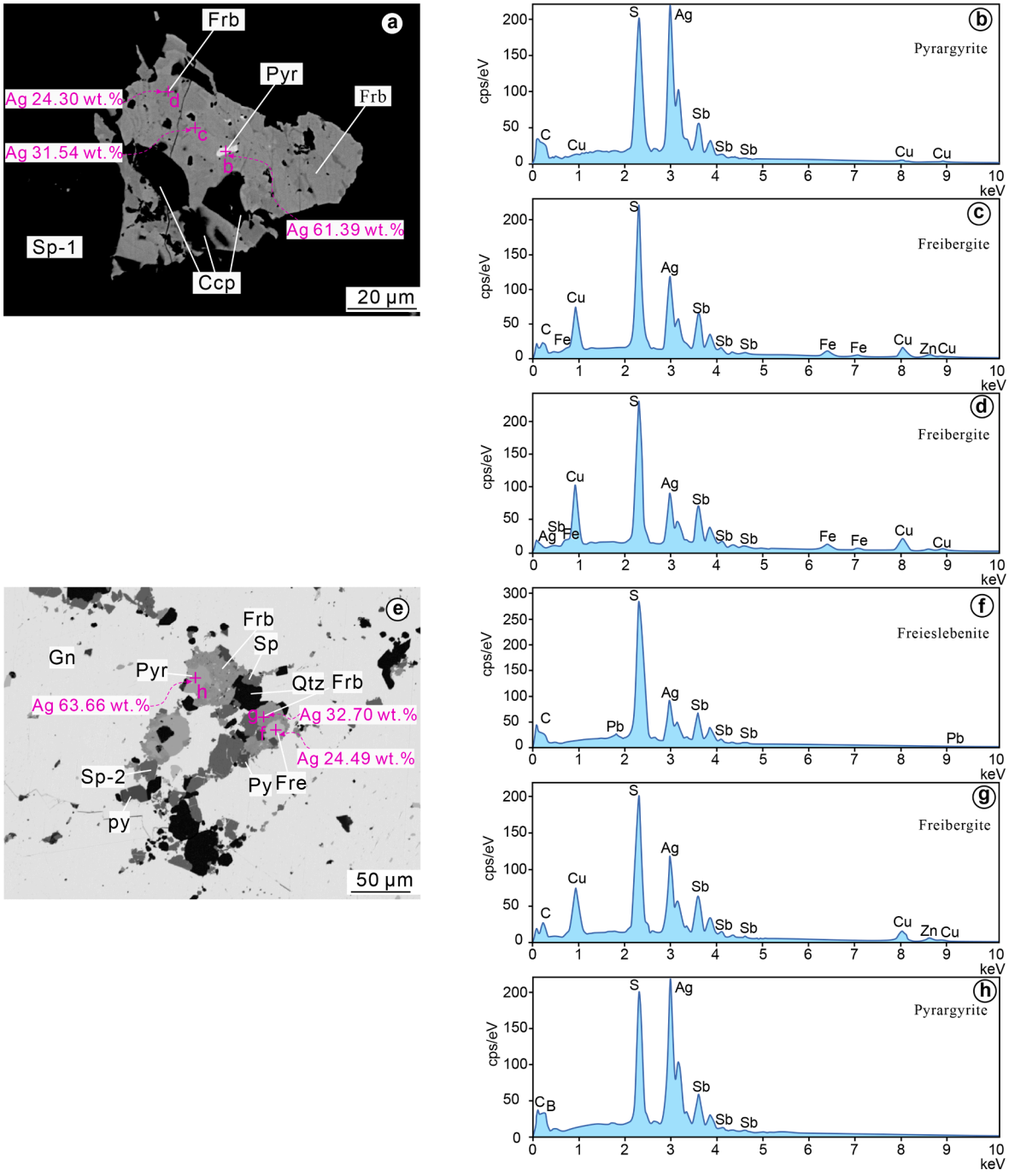

Fig. 7. BSE images (a and e) and EDS spectra (b–d and f–h) of Ag-bearing minerals. Spectra b–d corresponds to spot analysis in (a), and spectra f–h corresponds to spot analysis in (e).

(<1.91 wt%) contents, and the S and Fe contents are 31.30–33.23 wt% and 2.71–4.40 wt%, respectively. In addition, the bright zonation of Sp-1 in the BSE images shows higher Ag, Cu, and Sb contents than those of the darker zones (Fig. 6). Sp-2 coexists with Py-2 and shows a texture of chalcopyrite disease (Fig. 4d and e). In comparison to Sp-1, Sp-2 has higher Zn (60.99–65.57 wt%), lower S (32.95–33.49 wt%) and lower Fe (1.64–3.87 wt%) contents. Sp-2 has low Cu (<1.41 wt%), Ag (<0.10 wt %), and Sb (<0.02 wt%) contents.

Galena is present in substage II-2, occurring as irregular grains, replacing pyrite, sphalerite, chalcopyrite, and freibergite (Fig. 4d–h). Galena is primarily composed of Pb (85.65–86.73 wt%) and S (13.71–13.87 wt%) and has low Ag (<0.21 wt%) and Sb (<0.24 wt%) contents, along with trace amounts of Co, Ni, Fe, Cu, and Zn.

5.2.2. *Ag-bearing minerals*

Pyrargyrite has a diameter of 5–250 μm, occurring as irregular inclusions replacing galena, sphalerite, pyrite, and quartz (Fig. 4b, i, k). It contains 59.13–63.66 wt% Ag, 17.18–18.47 wt% S, and 12.80–21.69 wt % Sb. In addition, pyrargyrite has low contents of As (<5.37 wt%), Fe (<1.41 wt%), Zn (<0.93 wt%), Cu (<0.45 wt%), Pb (<0.41 wt%), Cd (<0.25 wt%), Bi (<0.12 wt%), and Au (0.11 wt%, one analysis only).

Freibergite occurs as inclusions or veinlets in sphalerite and galena,

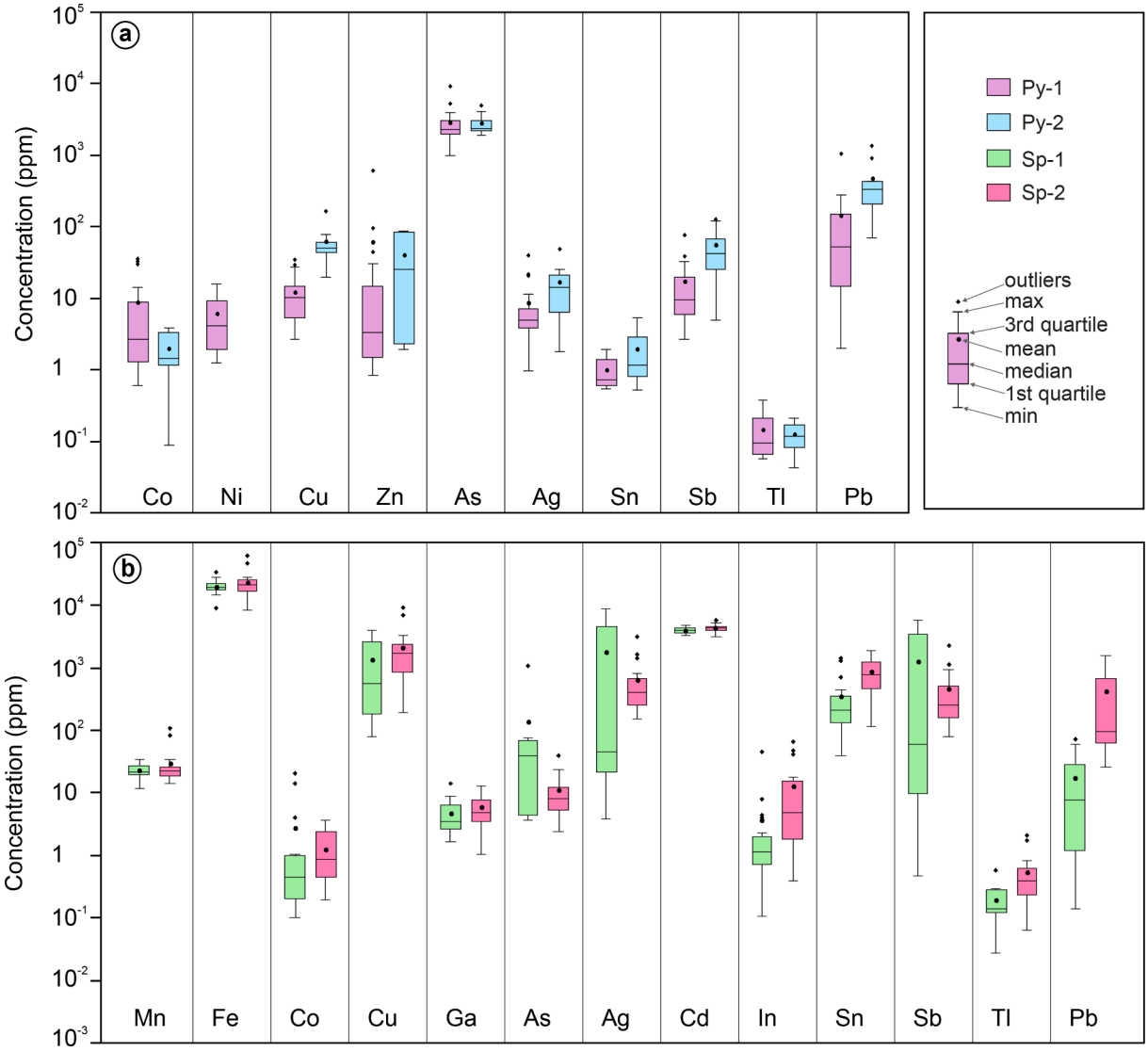

Fig. 8. Box and whisker plots showing the trace elements compositions of pyrite (a) and sphalerite (b) in the Wutuogou Ag-Pb-Zn deposit.

with diameters ranging from 4 to 120 μm (Fig. 4h, k, Fig. S1c). It is generally intergrown with chalcopyrite. The majority of the freibergite that coexists with sphalerite is heterogeneous and shows bright and dark zones in back-scattered electron (BSE) images (Fig. 7a, Fig. S1e). In contrast, freibergite occurring in galena is homogeneous (Fig. 7e). Freibergite has Ag, Cu, S, and Sb contents of 17.67–35.14 wt%, 13.32–25.41 wt%, 20.29–22.80 wt%, and 21.88–26.61 wt%, respectively. Significant variations in Zn (0.85–6.28 wt%) and Fe (0.60–5.13 wt%) are also detected. Freibergite has minor amounts of Cd (<0.33 wt %), As (<1.82 wt%), and Pb (<0.21 wt%). The brighter parts of the heterogeneous freibergite correspond to high Ag contents whereas the darker parts show low Ag contents (Fig. 7a, Fig. S1e).

Freieslebenite occurs as inclusions or exsolution inclusions in galena with diameters ranging from 3 to 80 μm (Fig. 4l, Fig. S1d, f). The freieslebenite contains 20.21–24.92 wt% Ag, 17.79–18.79 wt% S, 20.42–25.87 wt% Sb, and 29.02–39.40 wt% Pb. It has low Cu (<0.31 wt %), Zn (<0.37 wt%), Ge (<0.12 wt%), and Cd (<0.26 wt%) contents.

5.3. Sulfide trace element contents

The LA-ICP-MS dataset includes the trace element contents of sphalerite and pyrite. The reported mean concentrations for trace elements were calculated assuming that contents are zero for spot analyses below the detection limit (bdl). The trace element contents are listed in Table S3 and displayed in Fig. 8.

5.3.1. Pyrite

The As, Ag, and Sb contents in Py-1 are 5086–34932 ppm, 1.91–131 ppm, and 5.90–127 ppm (Fig. 8a), respectively. The contents of Zn, Cu, and Pb have wide ranges, with values varying from bdl to 358 ppm, 6.03–113 ppm, and 4.28–1194 ppm, respectively. Py-1 has a Co content of 1.11–116 ppm and a Ni content of bdl-46.3, corresponding to Co/Ni mass ratios of 1.1–8.9. Four of the 19 spot analyses revealed detectable Sn (0.97–5.64 ppm). The Pb, Zn, Ag, Sb, and Cu contents in Py-2 are higher than those in Py-1, ranging from bdl-7375 ppm, bdl-317 ppm, 3.82–165 ppm, 12.1–493 ppm, and 59.1 to 665 ppm, respectively (Fig. 8a). In addition, Py-2 contains 11066–32509 ppm As, 0.94–13.4 ppm Sn, and <40.8 ppm Co.

5.3.2. Sphalerite

Overall, Fe, Cu, Ag, Cd, Sn, Sb, and Pb are enriched in sphalerite (Sp-1 and Sp-2), but Mn, Co, Ga, Ge, Tl, and Bi are absent. The contents of Fe (9049–33764 ppm), Ag (3.86–8806 ppm), Sb (0.47–5855 ppm), and Pb (0.14–72.7 ppm) are variable in Sp-1, whereas the contents of Mn (11.6–35.1 ppm) and Cd (3335–4785 ppm) are not much varied (Fig. 8b). Sp-1 has high Cu (77.6–4074 ppm) and low In (0.11–44.7

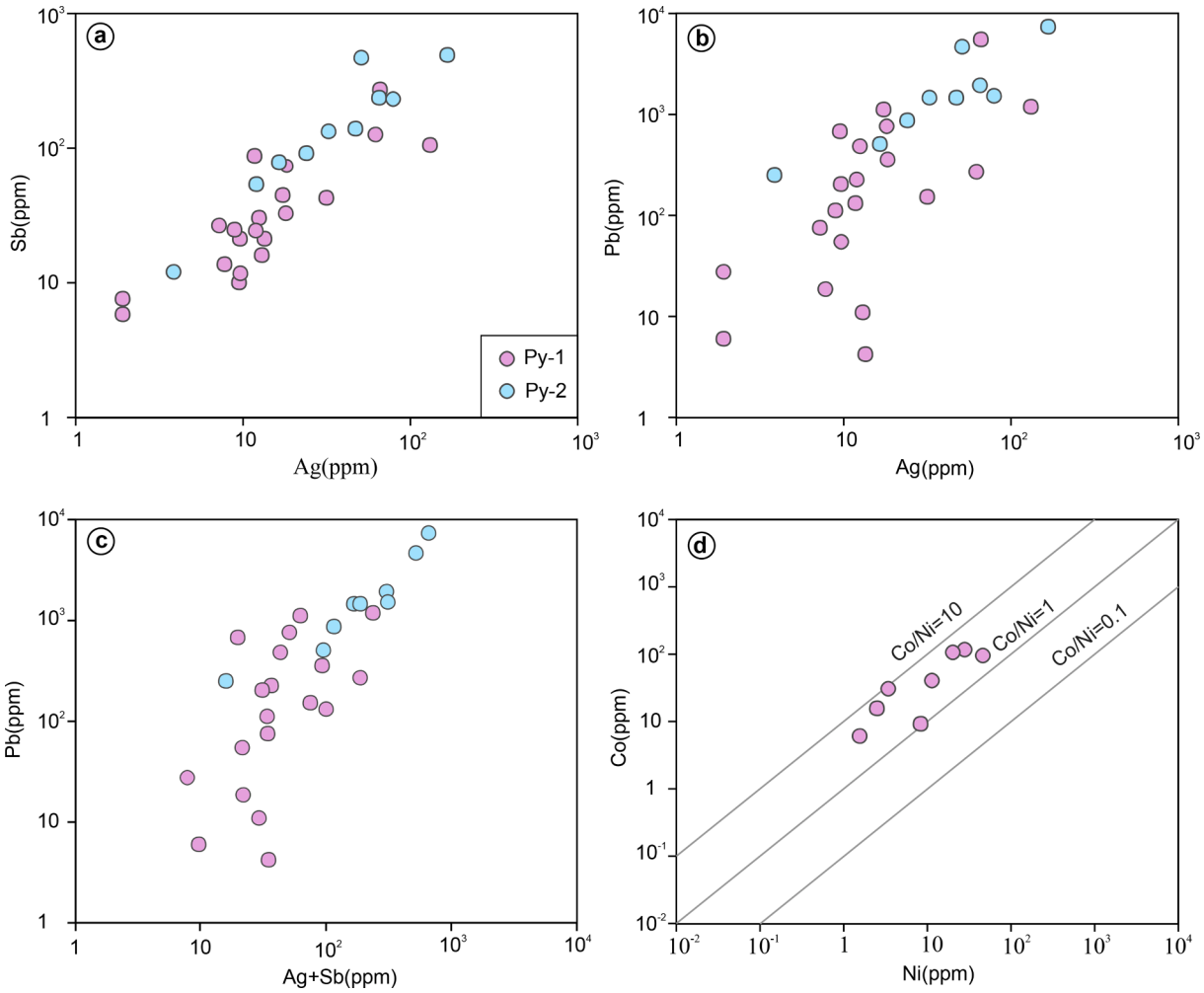

Fig. 9. Binary plots of (a) Sb vs. Ag; (b) Pb vs. Ag; (c) Sn vs. Ag; (d) Co vs. Ni in pyrite from Wutuogou Ag-Pb-Zn deposit.

ppm) contents. It has low Co (<20.3 ppm) and As (<76.3 ppm) contents, excluding an abnormally high As content (1060 ppm) for one analysis, which is probably related to the presence of an arsenopyrite inclusion. The Co (bdl-3.72 ppm), In (0.38–64.7 ppm), Sn (116–1920 ppm), and Pb (25.9–1551 ppm) contents in Sp-2 are more abundant than in Sp-1, whereas the Ag (151–3115 ppm) and Sb (79.9–2279 ppm) contents are lower (Fig. 8b). The Mn, Fe, Cu, Ga, and Cd contents in Sp-1 and Sp-2 are similar. In addition, two Sp-2 analyses revealed Ge contents of 5.05 ppm and 4.59 ppm, respectively.

5.4. *In-situ S isotopic compositions*

The sulfur isotopic compositions are presented in Table S4. The $\delta^{34}S$ values for stage I pyrite (Py-1) ranged from +6.13 to +7.78 ‰ (average of +7.06 ‰). Py-2, Sp-1, and Sp-2 of stage II have $\delta^{34}S$ values ranging from +5.75 to +6.66 ‰ (average of +6.14 ‰), +5.56 to +6.59 ‰ (average of +6.00 ‰), and +5.49 to +6.60 ‰ (average of +5.91 ‰), respectively.

6. Discussion

6.1. *Mineralization age*

The calcite (Cal-1) U-Pb analyses yield a lower intercept age of 210 ± 7 Ma on the Terra-Wasserburg diagram (Fig. 5d), indicating a Late Triassic mineralization age for the Wutuogou Ag-Pb-Zn deposit. This age is consistent with the timing of regional Ag-Pb-Zn mineralization in the EKOB. The formation ages of the Harizha Ag polymetallic deposit and the Nagengkangqieer North Ag deposit were 223 Ma and 218 Ma, respectively, restricted by hydrothermal zircon in ore-bearing quartz veins (Fan et al., 2021; Fan, 2022). The maximum ore-forming age (215 Ma) of the Nagengkangqieer Ag deposit was defined by the U-Pb age of hydrothermal zircon from mineralized rhyolites (Wu, 2019), and the minimum age of mineralization (207 ± 3 Ma) was determined from the U-Pb data analysis of a post-ore calcite vein established (Zhang et al., 2023a). In addition, Late Triassic magmatic events are prevailing in the EKOB, producing magma assemblages of diorite, granitoid, and rhyolite (Li et al., 2020b; Jing et al., 2023; Zhang et al., 2023b). These igneous rocks have been dated at 237–204 Ma by LA-ICP-MS and SHRIMP on zircon (Guo et al., 2018; Kong et al., 2020; Zhang et al., 2023b). The age of the Wutuogou deposit coincides with the Late Triassic magmatism in the EKOB, suggesting a potential connection.

6.2. *Distribution of silver*

In the Wutuogo Ag-Pb-Zn deposit, the distribution of silver in pyrargyrite (silver content ranging from 59.13 wt% to 63.66 wt%), freibergite (silver content ranging from 17.67 wt% to 35.14 wt%), freieslebenite (silver content ranging from 20.21 wt% to 24.68 wt%), and minor native silver indicates a significant presence of silver within Ag-bearing minerals. Furthermore, trace amounts of invisible silver are present in various sulfides, including galena, pyrite, and sphalerite, through different mechanisms.

Silver in pyrite typically occurs as micro-inclusions or solid solutions.

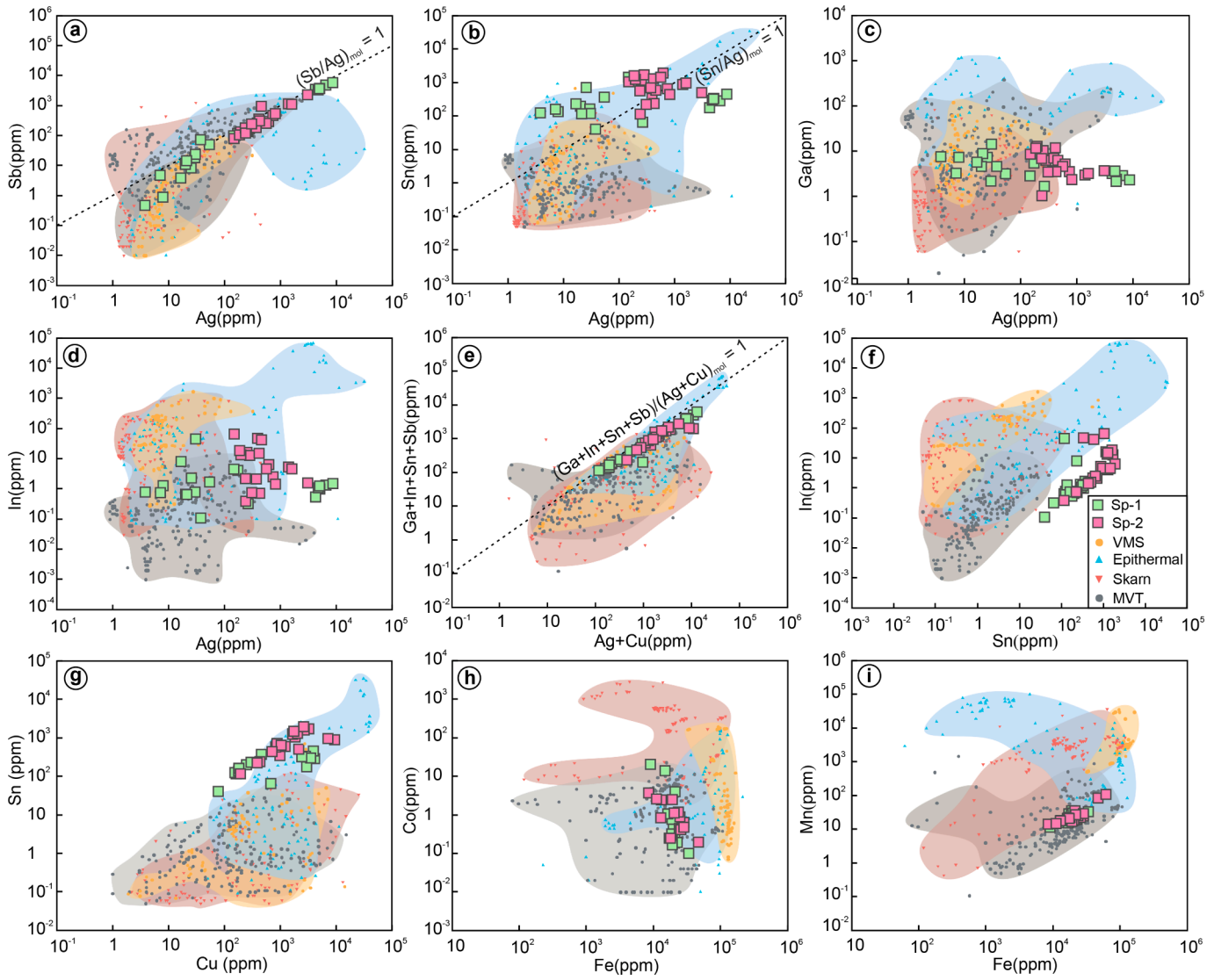

Fig. 10. Binary plots of (a) Sb vs. Ag; (b) Sn vs. Ag; (c) Ga vs. Ag; (d) In vs. Ag; (e) Ga + In + Sn + Sb vs. Ag + Cu; (f) In vs. Sn; (g) Sn vs. Cu; (h) Co vs. Fe; (i) Mn vs.Fe in sphalerite from Wutuogou Ag-Pb-Zn deposit and other deposit types (the data of skarn deposits, VMS deposits, epithermal deposits and MVT deposits are from Cook et al. (2008) and Ye et al. (2011).

However, high Ag content is often attributed to the presence of Ag-bearing mineral inclusions (Zhao et al., 2011; Qi et al., 2022). Galena precipitates faster than pyrite and Pb^{2+} has a larger radius than Fe^{2+}, so Pb often occurs as galena micro-inclusions in pyrite (Morse and Luther, 1999). The peaks of the Pb time-resolved profiles in pyrite provide evidence of this (Fig. S3a and b). The parallel Ag, Sb, and Pb peaks of time-resolved profiles (Fig. S3a) suggest that the origin of Ag and Sb in pyrite is from galena micro-inclusions containing Ag-Sb solid solutions or Ag-bearing sulfosalt micro-inclusions. Positive correlations between Ag, Sb, and Pb in pyrite (Fig. 9a–c) and the replacement of pyrite by galena and pyrargyrite (Fig. 4b) further support this.

Coupled substitution mechanisms usually lead to the enrichment of monovalent, trivalent, and tetravalent cations in sphalerite, such as Ag^{+}, Cu^{+}, Sb^{3+}, Ga^{3+}, In^{3+}, Bi^{3+}, Ge^{4+}, As^{3+}, and Sn^{4+} (Cook et al., 2009; Murakami and Ishihara, 2013). The contents of Ag^{+} and Cu^{+}, the two most common monovalent cations in the Wutuogou Ag-Pb-Zn deposit, are nearly equal to the total contents of trivalent and tetravalent cations (Fig. 10e). This indicates that Ag occurs in sphalerite (Sp-1 and Sp-2) through coupled substitution with trivalent or tetravalent cations. The smooth time-resolved profiles and positive correlation (with a slope of ~ 1) between Ag and Sb in sphalerite (Fig. S3c, Fig. 10a), as would be expected from the coupled substitution mechanism of $2\,Ag^{+} + Sb^{3+} \leftrightarrow 3\,Zn^{2+}$. Spot analyses with high Ag content tend to show high As contents, which suggests that $Ag^{+} + As^{3+} \leftrightarrow 2\,Zn^{2+}$ substitution occurs in sphalerite (Sp-1 and Sp-2). Additionally, the weak positive correlation between Ag and Sn in Sp-1 suggests they might have been limited by coupled substitutions with Zn^{2+} (Fig. 10b), i.e., $2\,Ag^{+} + Sn^{4+} \leftrightarrow 2\,Zn^{2+}$. The scattered relationship between Ag, Ga, and In excludes these elements for coupled substitution (Fig. 10c and d). It is worth mentioning that the smooth time-resolved profiles of the Sp-1 spot analyses with high Ag contents (4340–8806 ppm) indicate that Ag in these sphalerites occurs as solid solutions (Fig. S3c). Cook et al. (2009) reported a similar occurrence of high Ag contents (>10,000 ppm) in sphalerite from the Toyoha deposit in Japan. Furthermore, several spot analyses show parallel peaks of Ag, Sb, and Pb on the time-resolved profiles, reflecting the handful existence of Ag-bearing mineral micro-inclusions or galena micro-inclusions (Fig. S3d).

Silver can enter galena through the coupled substitution $Ag^{+} + Sb^{3+} \leftrightarrow 2\,Pb^{2+}$ (George et al., 2015), which is the predominant distribution mechanism in many Ag-Zn-Pb deposits (Horn et al., 2019; Cave et al., 2020; Li et al., 2022; Qi et al., 2022). Galena spot analyses with high Ag contents tend to show high Sb contents but relatively low Pb contents,

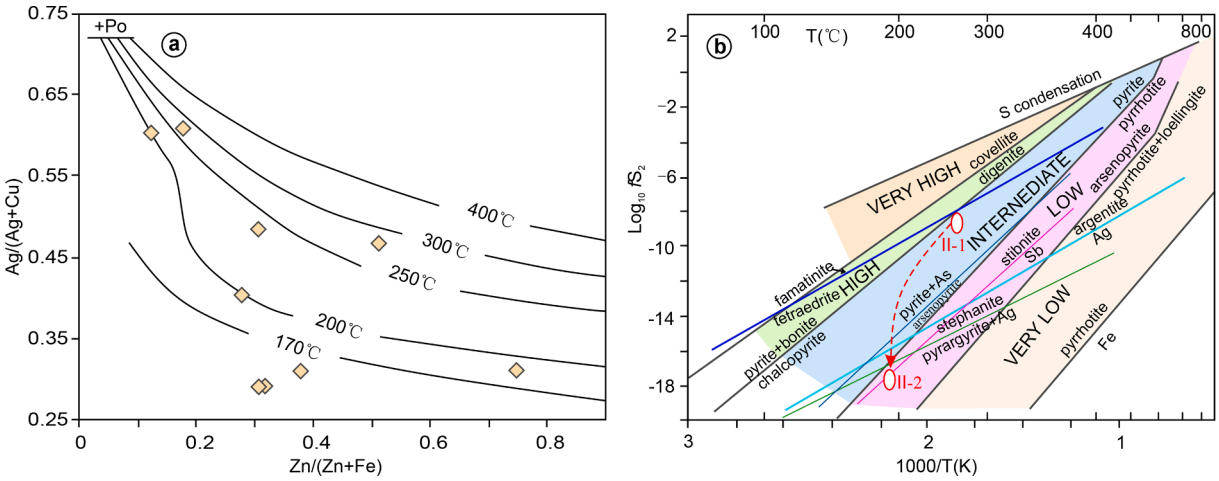

Fig. 11. (a) Ag/(Ag + Cu) vs. Zn/(Zn + Fe) mole ratios of freibergite in the Wutuogou Ag-Pb-Zn deposit. Based on Sack (2005), Zhai et al. (2019), and Li et al. (2019), the isotherms are computed. (b) The relative sulfidation condition and the evolution of hydrothermal fluids in the Wutuogou Ag-Pb-Zn deposit are shown in a $\log_{10}$ fS_2 vs. temperature diagram. The temperatures were estimated from the Fe/Zn ratio of sphalerite in substage II-1 and from the Ag/(Ag + Cu) and Zn/(Zn + Fe) ratio of freibergite in substage II-2. The mineral assemblage was used to estimate the $\log_{10}$ fS_2 values (see text for further discussion). Sulfidation conditions and reactions originate from Zhai et al. (2019).

suggesting that the occurrence of Ag and Sb in galena is indeed a result of the coupled substitution process ($Ag^+ + Sb^{3+} \leftrightarrow 2\ Pb^{2+}$) (Table S2).

In conclusion, silver (ranging from 1.91 to 165 ppm) is present as Ag-Sb-bearing inclusions in pyrite. The distribution of silver in sphalerite (ranging from 3.86 to 8806 ppm) can be attributed to two factors: (1) the presence of Ag-Sb-Pb micro-inclusions; (2) coupled substitution reactions, including $Ag^+ + Sb^{3+} \leftrightarrow 2\ Zn^{2+}$, with minor $Ag^+ + As^{3+} \leftrightarrow 2\ Zn^{2+}$, and $2\ Ag^+ + Sn^{4+} \leftrightarrow 3\ Zn^{2+}$. The silver content in galena (up to 0.21 wt%) forms solid solutions through coupled substitution ($Ag^+ + Sb^{3+} \leftrightarrow 2\ Pb^{2+}$).

6.3. Physicochemical conditions of mineralization

Deditius et al. (2014) discovered that Au and As contents were negatively correlated with fluid temperatures. The average As contents of Py-1 (14914 ppm) and Py-2 (17308 ppm) suggest that the fluid temperature at stage I is slightly higher than substage II-1. Previous studies have indicated that a high-temperature condition is required for the substitution of Co for Fe in pyrite (Clark et al., 2004; Román et al., 2019). The lower Co content in py2 (mean 2.97 ppm) compared to py1 (mean 24.6 ppm) also suggests a temperature decrease from stage I to substage II-1.

Sphalerite (Sp-1 and Sp-2) is common in substage II-1. It has been suggested that the Ga and In contents of sphalerite are temperature-dependent (Cook et al., 2009; Ye et al., 2011). Sphalerite with a low Ga/In mass ratio (<0.1) formed under a high-temperature condition, whereas sphalerite with a high Ga/In mass ratio (>1) generated at a moderate-to-low temperature condition (Cook et al., 2009; Ye et al., 2011). The Ga/In mass ratios of Sp-1 and Sp-2 range from 0.13 to 43.0 (mean of 3.67), indicating that they formed in a moderate-to-low temperature environment. The Ge contents in sphalerite show a positive correlation with the sphalerite crystallization temperature (Frenzel et al., 2016). Most of the Ge contents in Sp-1 and Sp-2 are below the detection limit, which also indicates a moderate-to-low temperature fluid. Keith et al. (2014) proposed the formula $Fe/Zn_{\ sphalerite} = 0.0013 \times T\ (°C) - 0.2953$ to calculate the ore-forming temperature from the sphalerite Fe/Zn mass ratios. The Fe/Zn mass ratios in substage II-1 sphalerite (Sp-1 and Sp-2) range from 0.025 to 0.075, indicating mineralization temperatures of 246–284 °C (mean of 266 °C) (Table S5). The composition of freibergite, which is widespread in substage II-2, can be used to determine the temperature of silver mineralization (Sack, 2005). Using the Ag/(Ag + Cu) and Zn/(Zn + Fe) mole ratios in unaltered freibergite, the mineralization temperature is estimated to be 140–270 °C in substage II-2 (Fig. 11a).

The mineral assemblage reflects the degree of sulfidation during mineralization. A pyrite-pyrrhotite-arsenopyrite and Fe-rich sphalerite assemblage indicates low-sulfidation conditions; a pyrite-tetrahedrite-chalcopyrite and Fe-poor sphalerite assemblage indicates medium-sulfidation conditions; and a pyrite-enargite-covellite assemblage indicates high-sulfidation conditions (Baumgartner et al., 2008). The Fe content of sphalerite is also closely related to the sulfur fugacity (fS_2), both of which are generally negatively correlated (Lusk and Calder, 2004; Demir et al., 2013; Keith et al., 2014). Pyrite, sphalerite (average Fe content of 21,779 ppm), chalcopyrite, and tetrahedrite (Fig. S2) are among the metallic sulfides found in substage II-1, indicating a medium-sulfidation environment. On the temperature vs. $\log_{10}$ fS_2 phase diagrams (Fig. 11b), the substage II-1 pyrite-chalcopyrite-tetrahedrite assemblage indicates a medium-to-low sulfidation condition at ~266 °C whereas the substage II-2 assemblage of Ag-sulfosalts indicates a low sulfidation environment at ~200 °C. As a result, the main mineralization stage II evolved from medium ($\log_{10}$ fS_2 of about −9) to low fS_2 conditions ($\log_{10}$ fS_2 of about −18). The narrow $\delta^{34}S$ range (+5.49 to +7.78 ‰) implies that the pH and oxygen fugacity (fO_2) did not significantly change during mineralization.

In summary, stage I mineralization occurred at a slightly higher temperature than stage II. Substage II-1 mineralization is characterized by a medium temperature (246–284 °C) and medium fS_2 ($\log_{10}$ fS_2 is about −9), whereas substage II-2 mineralization occurs at a low temperature (140–270 °C) and low fS_2 ($\log_{10}$ fS_2 is about −18). These findings indicate that cooling and a decrease in fS_2 cause the precipitation of Ag-bearing minerals.

6.4. Ore mineralogical and textural implications

Back-scattered electron images and EPMA revealed that freibergite has a heterogeneous composition (Fig. S1e, Fig. 7a) and that sphalerite (Sp-1) is characterized by Ag zonation (Fig. S1b, Fig. 6a). These phenomena may be the result of retrograde solid-state reactions. The heterogeneous freibergite was initially a homogeneous mineral hosted in sphalerite that underwent a microscale exsolution process to form Ag-rich and Ag-poor parts during cooling. The sphalerite, which shows Ag zonation, went through a similar process. This conclusion is supported by previous studies reporting similar phenomena (Sack et al., 2003; Zhai et al., 2019). The $Ag^+ + Sb^{3+} \leftrightarrow 2\ Zn^{2+}$ coupled substitution can be

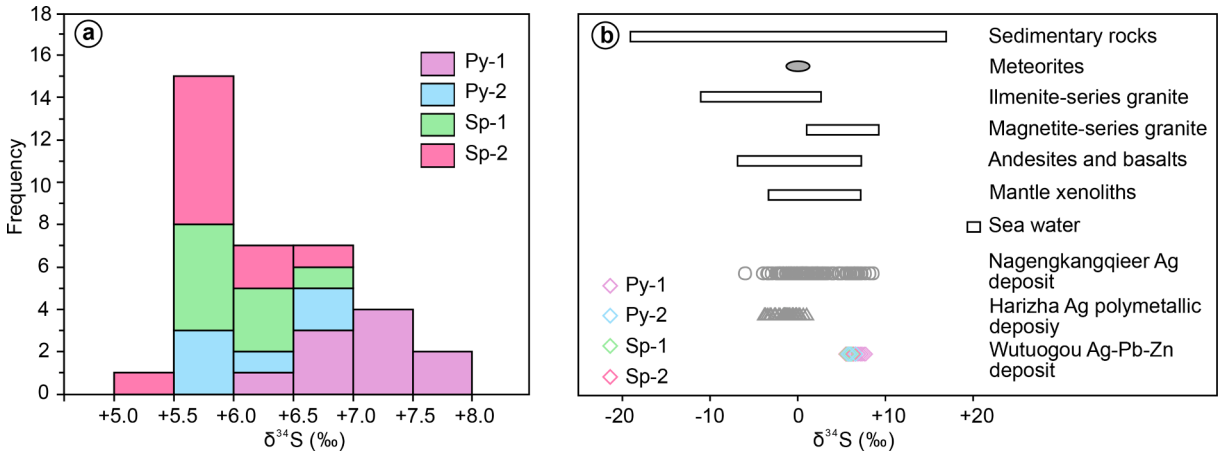

Fig. 12. (a) Histogram of $\delta^{34}S$ values. (b) Range of $\delta^{34}S$ values for pyrite and sphalerite in the Wutuogou Ag-Pb-Zn deposit. $\delta^{34}S$ data for the Nagengkanngqieer Ag deposit and the Harizha Ag polymetallic deposit are from Zhang et al. (2018), Xu et al. (2020), Chen et al., (2020b), Fan et al. (2021), Chen et al. (2022). The $\delta^{34}S$ values of sedimentary rocks, meteorites, ilmenite- and magnetite-series granites, andesites and basalts, and mantle xenoliths are from Seal (2006).

promoted by an Sb increase in the fluid during cooling, which contributes to the formation of Ag-zonation in sphalerite (Miller and Craig, 1983; Demir et al., 2013).

Galena contains exsolution inclusions of sulfosalts (Fig. S1f), indicating the initial presence of Ag-rich galena that transformed into Ag-poor galena and Ag-rich sulfosalts (e.g., freieslebenite) during cooling. This implies that the exsolution of Ag-rich sulfosalts accounts for the low Ag contents (<0.21 wt%) in galena. The replacement of galena by pyrargyrite suggests the formation of some Ag-bearing sulfosalts later than galena (Fig. 4k), reflecting late-stage low-temperature mineralization.

6.5. Genetic type of the Wutuogou Ag-Pb-Zn deposit

The trace element contents of sphalerite (i.e., Mn, Fe, Co, Ga, Ge, In, Cu, and Sn) can be used to determine the genetic type of ore deposit (Cook et al., 2009; Ye et al., 2011; Belissont et al., 2014). Sphalerite from deposits associated with magmatism tends to have higher contents of In, Sn, Fe, Co (especially in skarns), Mn, and Ag (e.g., the Toyoha deposit in Japan), whereas low-temperature deposits without a magmatic source (e.g., the MVT deposit) contain sphalerite that is enriched in Ge, As, Tl, Ga, and Se (Cook et al., 2009; Ye et al., 2011). The sphalerite in this study is enriched in In, Sn, Fe, Co, Ag, Sb, and Cu and depleted in Ge, Ga, Se, and Tl, like the sphalerite from magmatic-hydrothermal deposits (Fig. 10). The pyrite Co/Ni mass ratios are also valuable in determining deposit genesis (Large et al., 2009; Reich et al., 2013; Wei et al., 2020; Li et al., 2023). The VMS, skarn, and epithermal deposits related to magmatism typically exhibit pyrite Co/Ni mass ratios greater than 1, whereas Co/Ni mass ratios are often less than 1 in sedimentary pyrite. In this study, the pyrite has a Co/Ni mass ratio of 1.2–8.9 (Fig. 9d), indicating a magmatic-hydrothermal deposit type.

Sulfur isotope is one of the traditional methods to evaluate the source of ore-forming materials (Ohmoto, 1972). Equilibrium fractionation results in the following orders: $\delta^{34}S$ pyrite > $\delta^{34}S$ sphalerite > $\delta^{34}S$ chalcopyrite > $\delta^{34}S$ galena. The pyrite $\delta^{34}S$ in this study has a mean value of +6.71 ‰, which is higher than the mean $\delta^{34}S$ value of sphalerite (+5.95 ‰), indicating that fractionation equilibrium was reached. The lack of sulfate minerals and coexisting pyrite, sphalerite, and galena suggest a moderate to low fO_2, hence the $\delta^{34}S$ values of pyrite and sphalerite are equivalent to the $\delta^{34}S_{\sum S}$ (Ohmoto, 1972). The narrow $\delta^{34}S$ range indicates a single sulfur source in the Wutuogou Ag-Pb-Zn deposit. The $\delta^{34}S$ values of sulfide (+5.49 to +7.78 ‰, mean of +6.29 ‰) are higher than those of the Nagengkangqier Ag (−6.1 to +8.5 ‰, mean of +1.23 ‰ (Li and Li, 2017; Xu et al., 2020; Chen et al., 2020b) and the Hazhizha Ag polymetallic deposits (−3.8 to +1.0 ‰, mean of −1.45 ‰, (Fan et al., 2021)) (Fig. 12). Notably, the Nagengkangqier Ag and Hazhizha Ag polymetallic deposits are known to have a magmatic-hydrothermal origin (Chen et al., 2020b; Fan et al., 2021; Zhang et al., 2023a). The Wutuogou Ag-Pb-Zn deposit has higher $\delta^{34}S$ values that are comparable with magnetite-series granites (Fig. 12b), which suggests that sulfur was derived from felsic magmas. Conversely, the lower $\delta^{34}S$ values of Nagengkangqier Ag and Hazhizha Ag polymetallic deposits imply that some sulfur was likely derived from mantle-sourced input (Chen et al., 2020b; Zhang et al., 2023a).

The Zn/Cd mass ratios in sphalerite can provide insights into the origin of hydrothermal fluids (Khin and Large, 1996). High Zn/Cd mass ratios in sphalerite (>500) or moderate Zn/Cd mass ratios (328–427) typically indicate that the ore-forming hydrothermal fluids were derived from basaltic and andesitic sources (Gottesmann and Kampe, 2007). Conversely, a low Zn/Cd mass ratio in sphalerite (<250) is indicative of a felsic source (Khin and Large, 1996; Gottesmann and Kampe, 2007). In the case of the Wutuogou Ag-Pb-Zn deposit, the low Zn/Cd mass ratio (107–195) strongly suggests that the ore-forming fluids had a felsic magma source.

Considering the information provided, particularly the mineral assemblages, trace elements of pyrite and sphalerite, temperature (140 to 284 °C of main Stage II), and sulfur isotope data (+5.49 to +7.78 ‰), it is a reasonable conclusion that the Wutuogou Ag-Pb-Zn deposit can be classified as a medium-to-low-temperature magmatic-hydrothermal deposit with a genetic association to felsic magmas.

6.6. Formation of the Wutuogou deposit

Based on the geological and geochronological data presented, it appears that the granodiorite and monzogranite host rocks were formed earlier, at around 248 Ma and 246 Ma (Li et al., 2018), respectively, whereas the deposit itself was formed during the Late Triassic, approximately 210 Ma. This geochronological relationship suggests that the granodiorite and monzogranite are not the source of the ore-forming materials for the deposit.

Since 240 Ma, the Paleo-Tethys Ocean has been beginning to close (Zhao et al., 2022b; Zhang et al., 2023b). This was subsequently followed by the post-collision extension of the EKOB from 224 Ma to 200 Ma, along with upwelling of the asthenosphere mantle and large-scale magmatism (Kong et al., 2020; Chen et al., 2020a; Li et al., 2020c; Zhao et al., 2022a). Although the Late Triassic magmatic rocks have not been discovered in the Wutuogou area, they are prevalent in the eastern segment of the EKOB (Guo et al., 2018; Jing et al., 2023; Zhang et al., 2023b). We hypothesize that a Late Triassic felsic pluton, situated deep beneath the Wutuogou area, served as the source of ore-forming fluids,

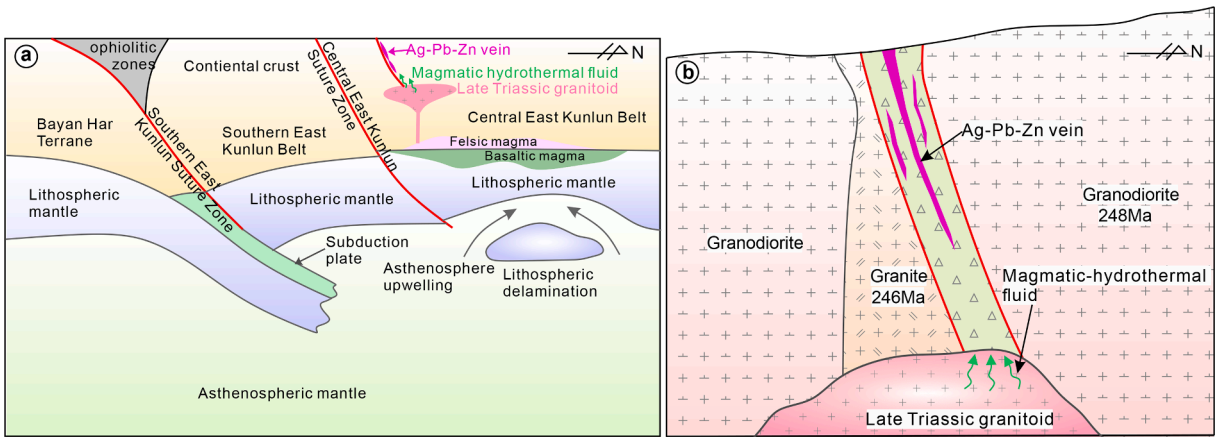

Fig. 13. Geological setting (a) and genetic model (b) for the Wutuogou Ag-Pb-Zn deposit. The age of granodiorite and monzogranite are from Li et al. (2018).

materials, and the thermal energy required for the formation of the Wutuogou Ag-Pb-Zn deposit. These ore-forming fluids followed pre-existing fault structures, like the F8 fault depicted in Fig. 2, eventually reaching shallower depths where silver mineralization took place. Subsequently, a decrease in fS_2 and the cooling of the mineralizing fluids resulted in the formation of the Wutuogou Ag-Pb-Zn deposit in ~210 Ma (Fig. 13).

7. Conclusions

(1) Three hydrothermal mineralization stages are recognized in the Wutuogou Ag-Pb-Zn deposit. Stage I is characterized by quartz-pyrite (Py-1)-arsenopyrite. Stage II can be further divided into substages II-1 and II-2. Substage II-1 is defined by pyrite (Py-2)-sphalerite-chalcopyrite-tetrahedrite-quartz, while substage II-2 is characterized by galena-smithsonite-pyrargyrite-freibergite-freieslebenite-quartz-calcite. Stage III primarily consists of quartz and calcite.

(2) The majority of silver is present in Ag-bearing minerals such as pyrargyrite, freibergite, and freieslebenite. Furthermore, invisible silver occurs in pyrite (2–165 ppm), sphalerite (4–8806 ppm), and galena (up to 0.21 wt%) as solid solutions that resulted from coupled substitution ($Ag^+ + Sb^{3+} \leftrightarrow 2\,Zn^{2+}$, $Ag^+ + Sb^{3+} \leftrightarrow 2\,Pb^{2+}$) or micro-scale inclusions. Cooling and a decrease in the fS_2 of the ore-forming fluid are the main causes of Ag mineralization. Heterogeneous freibergite and Ag-zonation in sphalerite are attributed to retrograde solid-state reactions during cooling.

(3) Based on trace element data from pyrite and sphalerite, sulfur isotopic compositions (+5.49 to +7.78 ‰), and estimated fluid temperatures (ranging from 140 to 284 °C), the Wutuogou Ag-Pb-Zn deposit is classified as a medium- to low-temperature magmatic-hydrothermal deposit connected to Late Triassic magmatism in the EKOB. Its mineralization age (low limit) is determined to be 210 ± 7 Ma by calcite U-Pb dating.

Declaration of competing interest

The authors declare that they have no known competing financial interests or personal relationships that could have appeared to influence the work reported in this paper.

Data availability

Data will be made available on request.

Acknowledgments

This study was supported by the National Natural Science Foundation of China (No. 42172084). We would like to thank Shengtao Zhang, Xiaolong Li, and Bin Li for their assistance with fieldwork. We extend our gratitude to the editor and three reviewers for their valuable insights and suggestions.

Appendix A. Supplementary data

Supplementary data to this article can be found online at https://doi.org/10.1016/j.oregeorev.2024.105880.

References

Baumgartner, R., Fontbote, L., Vennemann, T., 2008. Mineral zoning and geochemistry of epithermal polymetallic Zn-Pb-Ag-Cu-Bi mineralization at Cerro de Pasco, Peru. Econ. Geol. 103 (3), 493–537. https://doi.org/10.2113/gsecongeo.103.3.493.

Beaudoin, G., Sangster, D.F., 1992. A descriptive model for silver-lead-zinc veins in clastic metasedimentary terranes. Econ. Geol. 87 (4), 1005–1021. https://doi.org/10.2113/gsecongeo.87.4.1005.

Belissont, R., Boiron, M., Luais, B., Cathelineau, M., 2014. LA-ICP-MS analyses of minor and trace elements and bulk Ge isotopes in zoned Ge-rich sphalerites from the Noailhac-Saint-Salvy deposit (France): Insights into incorporation mechanisms and ore deposition processes. Geochim. Cosmochim. Ac. 126, 518–540. https://doi.org/10.1016/j.gca.2013.10.052.

Box, S.E., Bookstrom, A.A., Anderson, R.G., 2012. Origins of mineral deposits, Belt-Purcell Basin, United States and Canada; an introduction. Econ. Geol. 107 (6), 1081–1088. https://doi.org/10.2113/econgeo.107.6.1081.

Burisch, M., Walter, B.F., Gerdes, A., Lanz, M., Markl, G., 2018. Late-stage anhydrite-gypsum-siderite-dolomite-calcite assemblages record the transition from a deep to a shallow hydrothermal system in the Schwarzwald mining district, SW Germany. Geochim. Cosmochim. Ac. 223, 259–278. https://doi.org/10.1016/j.gca.2017.12.002.

Catchpole, H., Kouzmanov, K., Bendezú, A., Ovtcharova, M., Spikings, R., Stein, H., Fontboté, L., 2015. Timing of porphyry (Cu-Mo) and base metal (Zn-Pb-Ag-Cu) mineralisation in a magmatic-hydrothermal system—Morococha district, Peru. Miner. Deposita. 50 (8), 895–922. https://doi.org/10.1007/s00126-014-0564-x.

Cave, B., Lilly, R., Barovich, K., 2020. Textural and geochemical analysis of chalcopyrite, galena and sphalerite across the Mount Isa Cu to Pb-Zn transition: implications for a zoned Cu-Pb-Zn system. Ore Geol. Rev. 124, 103647 https://doi.org/10.1016/j.oregeorev.2020.103647.

Chen, X.D., Li, Y.G., Li, M.T., Zhou, H.B., Sun, C.B., Zhao, Y.C., Lai, C.K., 2020b. Ore geology, fluid inclusions, and C-H-O-S-Pb isotopes of Nagengkangqieergou Ag-polymetallic deposit, East Kunlun Orogen, NW China. Geol. J. 55 (4), 2572–2590. https://doi.org/10.1002/gj.3526.

Chen, X.D., Li, B., Tang, L., Zhang, W.D., Zhu, L., 2022. Silver enrichment and trace element deportment in hydrothermal replacement reactions: perspective from the Nageng Ag-polymetallic deposit, East Kunlun Orogen, NW China. Ore Geol. Rev. 142, 104691 https://doi.org/10.1016/j.oregeorev.2021.104691.

Chen, Y.X., Pei, X.Z., Li, Z.C., Li, R., Liu, C.G., Wang, M., 2017b. Magmatic events recorded in granitic gneisses from the Hatu area, eastern East Kunlun Orogen: response to the assembly of Rodinia. Geol. J. 52 (4), 403–418. https://doi.org/10.1002/gj.3006.

Chen, J.J., Wei, J.H., Fu, L.B., Li, H., Zhou, H.Z., Zhao, X., Zhan, X.F., Tan, J., 2017a. Multiple sources of the Early Mesozoic Gouli batholith, Eastern Kunlun Orogenic Belt, northern Tibetan Plateau: Linking continental crustal growth with oceanic

subduction. Lithos 292–293, 161–178. https://doi.org/10.1016/j.lithos.2017.09.006.
Chen, J.J., Fu, L.B., Wei, J.H., Selby, D., Zhang, D.H., Zhou, H.Z., Zhao, X., Liu, Y., 2020a. Proto-Tethys magmatic evolution along northern Gondwana: insights from Late Silurian-Middle Devonian A-type magmatism, East Kunlun Orogen, Northern Tibetan Plateau, China. Lithos. 356–357, 105304 https://doi.org/10.1016/j.lithos.2019.105304.
Clark, C., Grguric, B., Mumm, A.S., 2004. Genetic implications of pyrite chemistry from the Palaeoproterozoic Olary Domain and overlying Neoproterozoic Adelaidean sequences, northeastern South Australia. Ore Geol. Rev. 25 (3), 237–257. https://doi.org/10.1016/j.oregeorev.2004.04.003.
Coogan, L.A., Parrish, R.R., Roberts, N.M.W., 2016. Early hydrothermal carbon uptake by the upper oceanic crust; insight from in situ U-Pb dating. Geology (boulder). 44 (2), 147–150. https://doi.org/10.1130/G37212.1.
Cook, N.J., Ciobanu, C.L., Pring, A., Skinner, W., Shimizu, M., Danyushevsky, L., Saini-Eidukat, B., Melcher, F., 2009. Trace and minor elements in sphalerite: A LA-ICPMS study. Geochim. Cosmochim. Ac. 73 (16), 4761–4791. https://doi.org/10.1016/j.gca.2009.05.045.
Demir, Y., Uysal, İ., Sadıklar, M.B., 2013. Mineral chemical investigation on sulfide mineralization of the Istala deposit, Gümüşhane, NE-Turkey. Ore Geol. Rev. 53, 306–317. https://doi.org/10.1016/j.oregeorev.2013.01.014.
Dong, Y.P., He, D.F., Sun, S.S., Liu, X.M., Zhou, X.H., Zhang, F.F., Yang, Z., Cheng, B., Zhao, G.C., Li, J.H., 2018. Subduction and accretionary tectonics of the East Kunlun orogen, western segment of the Central China Orogenic System. Earth Sci. Rev. 186, 231–261. https://doi.org/10.1016/j.earscirev.2017.12.006.
Dong, Y.P., Sun, S.S., Santosh, M., Hui, B., Sun, J.P., Zhang, F.F., Cheng, B., Yang, Z., Shi, X.H., He, D.F., Yang, L., Cheng, C., Liu, X.M., Zhou, X.H., Wang, W., Qi, N., 2022. Cross Orogenic Belts in Central China: Implications for the tectonic and paleogeographic evolution of the East Asian continental collage. Gondw. Res. 109, 18–88. https://doi.org/10.1016/j.gr.2022.04.012.
Drake, H., Roberts, N.M.W., Whitehouse, M.J., 2020. Geochronology and stable isotope analysis of fracture-fill and karst mineralization reveal sub-surface paleo-fluid flow and microbial activity of the COSC-1 borehole. Scand. Caledonides. Geosci. 10 (2), 56. https://doi.org/10.3390/geosciences10020056.
Fan, X.Z., Sun, F.Y., Xu, C.H., Xin, W., Wang, Y.C., Zhang, Y., 2021. Genesis of Harizha Ag-Pb-Zn deposit in the eastern Kunlun Orogen, NW China: evidence of fluid inclusions and C-H-O-S-Pb isotopes. Resour. Geol. 71 (3), 177–201. https://doi.org/10.1111/rge.12256.
Fan, X.Z., 2022. Research on metallogenesis of Ag Polymetallic deposits in the east segment of the East Kunlun Orogenic Belt, Qinghai Province (Ph.D. thesis). Jilin University. 292p (in Chinese with English Abstract).
Fang, J., Zhang, L., Chen, H.Y., Zheng, Y., Li, D.F., Wang, C.M., Shen, D.L., 2018. Genesis of the Weibao banded skarn Pb-Zn deposit, Qimantagh, Xinjiang: Insights from skarn mineralogy and muscovite 40Ar-39Ar dating. Ore Geol. Rev. 100, 483–503. https://doi.org/10.1016/j.oregeorev.2017.06.001.
Frenzel, M., Hirsch, T., Gutzmer, J., 2016. Gallium, germanium, indium, and other trace and minor elements in sphalerite as a function of deposit type — a meta-analysis. Ore Geol. Rev. 76, 52–78. https://doi.org/10.1016/j.oregeorev.2015.12.017.
Fu, L.B., Bagas, L., Wei, J.H., Chen, Y., Chen, J.J., Zhao, X., Zhao, Z.X., Li, A.B., Zhang, W.K., 2022. Growth of early Paleozoic continental crust linked to the Proto-Tethys subduction and continental collision in the East Kunlun Orogen, northern Tibetan Plateau. GSA Bull. 135 (7–8), 1709–1733. https://doi.org/10.1130/B36292.1.
George, L., Cook, N.J., Ciobanu, C.L., Wade, B.P., 2015. Trace and minor elements in galena: a reconnaissance LA-ICP-MS study. Am. Mineral. 100 (2–3), 548–569. https://doi.org/10.2138/am-2015-4862.
Gottesmann, W., Kampe, A., 2007. Zn/Cd ratios in calcsilicate-hosted sphalerite ores at Tumurtijn-ovoo, Mongolia. Geochemistry 67 (4), 323–328. https://doi.org/10.1016/j.chemer.2007.01.002.
Guo, X.Z., Li, Y.Z., Jia, Q.Z., Li, J.C., Kong, H.L., Namkha, N., 2018. Geochronology and geochemistry of the Wulonggou orefield related granites in Late Permian-Triassic East Kunlun: implication for metallogenic tectonic. Acta Petrol. Sin. 34 (08), 2359–2379 (in Chinese with English abstract).
Horn, S., Dziggel, A., Kolb, J., Sindern, S., 2019. Textural characteristics and trace element distribution in carbonate-hosted Zn-Pb-Ag ores at the Paleoproterozoic Black Angel deposit, central West Greenland. Miner. Deposita 54 (4), 507–524. https://doi.org/10.1007/s00126-018-0821-5.
Hu, Z.C., Zhang, W., Liu, Y.S., Gao, S., Li, M., Zong, K.Q., Chen, H.H., Hu, S.H., 2015. "Wave" signal-smoothing and mercury-removing device for laser ablation quadrupole and multiple collector ICPMS analysis: application to lead isotope analysis. Anal. Chem. 87 (2), 1152–1157. https://doi.org/10.1021/ac503749k.
Huang, H., Niu, Y.L., Nowell, G., Zhao, Z.D., Yu, X.H., Zhu, D.C., Mo, X.X., Ding, S., 2014. Geochemical constraints on the petrogenesis of granitoids in the East Kunlun Orogenic belt, northern Tibetan Plateau: implications for continental crust growth through syn-collisional felsic magmatism. Chem. Geol. 370, 1–18. https://doi.org/10.1016/j.chemgeo.2014.01.010.
Jin, X.Y., Zhao, J.X., Feng, Y.X., Hofstra, A.H., Deng, X.D., Zhao, X.F., Li, J.W., 2021. Calcite U-Pb dating unravels the age and hydrothermal history of the giant Shuiyindong carlin-type gold deposit in the golden triangle, South China. Econ. Geol. 116 (6), 1253–1265. https://doi.org/10.5382/econgeo.4870.
Jing, G.Z., Wang, X.Y., Zhang, Z.Q., He, J.J., Zhang, L.B., Wang, F.L., Liu, Y., Shi, W.J., Tan, J., 2023. Middle-Late Triassic regional-scale magmatic-hydrothermal metallogenic system in the eastern segment of the East Kunlun. Bull. Geol. Sci. Technol. 42 (01), 89–111 (in Chinese with English abstract).
Keith, M., Haase, K.M., Schwarz-Schampera, U., Klemd, R., Petersen, S., Bach, W., 2014. Effects of temperature, sulfur, and oxygen fugacity on the composition of sphalerite from submarine hydrothermal vents. Geology (boulder). 42 (8), 699–702. https://doi.org/10.1130/G35655.1.
Kendrick, M.A., Plümper, O., Zhao, J., Feng, Y., Defliese, W.F., Müller, I.A., Ziegler, M., 2022. Exhumation and carbonation of the Atlantis Bank core complex constrained by in situ U-Pb dating and Δ47 thermometry of calcite veins, SW Indian Ridge. Earth Planet Sci. Lett. 584, 117474 https://doi.org/10.1016/j.epsl.2022.117474.
Khin, Z., Large, R.R., 1996. Petrology and geochemistry of sphalerite from the Cambrian VHMS deposits in the Rosebery-Hercules District, western Tasmania; implications for gold mineralisation and Devonian metamorphic-metasomatic processes. Miner. Petrol. 57 (1–2), 97–118. https://doi.org/10.1007/BF01161624.
Kissin, S.A., Mango, H., 2014. Silver Vein Deposits. In: Holland, H.D., Turekian, K.K. (Eds.), Treatise on Geochemistry, second ed. Elsevier, Oxford, pp. 425–432.
Kong, J.J., Niu, Y.L., Hu, Y., Zhang, Y., Shao, F.L., 2020. Petrogenesis of the Triassic granitoids from the East Kunlun Orogenic Belt, NW China: implications for continental crust growth from syn-collisional to post-collisional setting. Lithos 364–365, 105513. https://doi.org/10.1016/j.lithos.2020.105513.
Large, R.R., Danyushevsky, L., Hollit, C., Maslennikov, V., Meffre, S., Gilbert, S., Bull, S., Scott, R., Emsbo, P., Thomas, H., Singh, B., Foster, J., 2009. Gold and trace element zonation in pyrite using a laser imaging technique; implications for the timing of gold in orogenic and carlin-style sediment-hosted deposits. Econ. Geol. 104 (5), 635–668. https://doi.org/10.2113/gsecongeo.104.5.635.
Lawley, C.J.M., Richards, J.P., Anderson, R.G., Creaser, R.A., Heaman, L.M., 2010. Geochronology and geochemistry of the MAX porphyry Mo deposit and its relationship to Pb-Zn-Ag mineralization, Kootenay Arc, southeastern British Columbia, Canada. Econ. Geol. 105 (6), 1113–1142. https://doi.org/10.2113/econgeo.105.6.1113.
Li, M.T., Li, Z.Q., 2017. Constrains of S-Pb-C-O isotope compositions on the origin of Nagengkangqieer Silver Deposit, the Eastern Kunlun Mountains, China. Acta Mineral. Sin. 37(6), 771–781 (in Chinese with English abstract).
Li, J., Bi, S., Selby, D., Chen, L., Vasconcelos, P., Thiede, D., Zhou, M., Zhao, X., Li, Z., Qiu, H., 2012. Giant Mesozoic gold provinces related to the destruction of the North China craton. Earth Planet Sc. Lett. 349–350, 26–37. https://doi.org/10.1016/j.epsl.2012.06.058.
Li, Z.K., Li, J.W., Cooke, D.R., Danyushevsky, L., Zhang, L., O Brien, H., Lahaye, Y., Zhang, W., Xu, H.J., 2016. Textures, trace elements, and Pb isotopes of sulfides from the Haopinggou vein deposit, southern North China Craton: implications for discrete Au and Ag–Pb–Zn mineralization. Contrib. Miner. Petrol. 171 (12) https://doi.org/10.1007/s00410-016-1309-x.
Li, R.B., Pei, X.Z., Li, Z.C., Pei, L., Chen, G.C., Chen, Y.X., Liu, C.J., Wang, S.M., 2018. Paleo-Tethys Ocean subduction in eastern section of East Kunlun Orogen: evidence from the geochronology and geochemistry of the Wutuo pluton. Acta Petrol. Sin. 34 (11), 3399–3421 (in Chinese with English abstract).
Li, H.R., Qian, Y., Sun, F.Y., Sun, J.L., Wang, G., 2020a. Zircon U-Pb dating and sulfide Re–Os isotopes of the Xiarihamu Cu–Ni sulfide deposit in Qinghai Province, Northwestern China. Can. J. Earth Sci. 57 (8), 885–902. https://doi.org/10.1139/cjes-2019-0107.
Li, Y.J., Wei, J.H., Ulrich, T., Chen, M.T., Li, H.M., Niu, M.W., Liu, B., 2019. Mineral chemistry of the Xiasai Ag-Pb-Zn deposit in the central Yidun Terrane, SW China: insight into Ni-Ag-Bi mineralization and formation conditions. Ore Geol. Rev. 114, 103136 https://doi.org/10.1016/j.oregeorev.2019.103136.
Li, Y.J., Wei, J.H., Tan, J., Fu, L.B., Li, H., Ke, K.J., 2020b. Albian-Cenomanian A-type granite-related Ag-Pb-Zn veins in the central Yidun Terrane, SW China: constraints from the Xiasai deposit. Miner. Deposita 55 (6), 1047–1070. https://doi.org/10.1007/s00126-019-00920-5.
Li, Y.J., Wei, J.H., Santosh, M., Li, H., Liu, H.W., Niu, M.W., Liu, B., 2020c. Anisian granodiorites and mafic microgranular enclaves in the eastern Kunlun Orogen, NW China: insights into closure of the eastern Paleo-Tethys. Geol. J. 55 (9), 6487–6507. https://doi.org/10.1002/gj.3814.
Li, Y.J., Wei, J.H., Chen, M.T., Chen, Z.H., Lahaye, Y., Zhang, H.J., Ulrich, T., 2023. Molybdenum mineralization genetically linked with magmatism at the Shipingchuan deposit, SE China. GSA Bull. 135 (11–12), 3112–3127. https://doi.org/10.1130/B36600.1.
Li, G.M., Zhao, Z.X., Wei, J.H., Ulrich, T., 2022. Trace element compositions of galena in an MVT deposit from the Sichuan-Yunnan-Guizhou metallogenic province, SW China: constraints from LA-ICP-MS spot analysis and elemental mapping. Ore Geol. Rev. 150, 105123 https://doi.org/10.1016/j.oregeorev.2022.105123.
Ludwig, K.R., 2003. Isoplot 3.00: A Geochronological Toolkit for Microsoft Excel, Berkeley. Berkeley Geochronology Center Special Publication.
Luo, K., Zhou, J.X., Feng, Y.X., Uysal, I.T., Nguyen, A., Zhao, J.X., Zhang, J.W., 2020. In situ U-Pb dating of calcite from the South China antimony metallogenic belt. iScience 23 (10), 101575. https://doi.org/10.1016/j.isci.2020.101575.
Lusk, J., Calder, B.O.E., 2004. The composition of sphalerite and associated sulfides in reactions of the Cu-Fe-Zn-S, Fe-Zn-S and Cu-Fe-S systems at 1 bar and temperatures between 250 and 535 °C. Chem. Geol. 203 (3–4), 319–345. https://doi.org/10.1016/j.chemgeo.2003.10.011.
Mango, H., Arehart, G., Oreskes, N., Zantop, H., 2014. Origin of epithermal Ag-Au-Cu-Pb-Zn mineralization in Guanajuato. Mexico. Miner. Deposita 49 (1), 119–143. https://doi.org/10.1007/s00126-013-0478-z.
Mederer, J., Moritz, R., Zohrabyan, S., Vardanyan, A., Melkonyan, R., Ulianov, A., 2014. Base and precious metal mineralization in Middle Jurassic rocks of the Lesser Caucasus: a review of geology and metallogeny and new data from the Kapan, Alaverdi and Mehmana districts. Ore Geol. Rev. 58, 185–207. https://doi.org/10.1016/j.oregeorev.2013.10.007.
Mehrabi, B., Siani, M.G., Goldfarb, R., Azizi, H., Ganerod, M., Marsh, E.E., 2016. Mineral assemblages, fluid evolution, and genesis of polymetallic epithermal veins, Glojeh

district, NW Iran. Ore Geol. Rev. 78, 41–57. https://doi.org/10.1016/j.oregeorev.2016.03.016.
Miller, J.W., Craig, J.R., 1983. Tetrahedrite-tennantite series compositional variations in the Cofer Deposit, Mineral District, Virginia. Am. Mineral. 68 (1–2), 227–234.
Morse, J.W., Luther, G.W., 1999. Chemical influences on trace metal-sulfide interactions in anoxic sediments. Geochim. Cosmochim. Ac. 63 (19), 3373–3378. https://doi.org/10.1016/S0016-7037(99)00258-6.
Murakami, H., Ishihara, S., 2013. Trace elements of Indium-bearing sphalerite from tin-polymetallic deposits in Bolivia, China and Japan: a femto-second LA-ICPMS study. Ore Geol. Rev. 53, 223–243. https://doi.org/10.1016/j.oregeorev.2013.01.010.
Nuriel, P., Wotzlaw, J.F., Ovtcharova, M., Vaks, A., Stremtan, C., Šala, M., Roberts, N.M.W., Kylander-Clark, A.R.C., 2021. The use of ASH-15 flowstone as a matrix-matched reference material for laser-ablation U-Pb geochronology of calcite. Geochronology 3 (1), 35–47. https://doi.org/10.5194/gchron-3-35-2021.
Ohmoto, H., 1972. Systematics of sulfur and carbon isotopes in hydrothermal ore deposits. Econ. Geol. 67 (5), 551–578. https://doi.org/10.2113/gsecongeo.67.5.551.
Pan, G.T., Wang, L.Q., Li, R.S., Yuan, S.H., Ji, W.H., Yin, F.G., Zhang, W.P., Wang, B.D., 2012. Tectonic evolution of the Qinghai-Tibet Plateau. J. Asian Earth Sci. 53, 3–14. https://doi.org/10.1016/j.jseaes.2011.12.018.
Paton, C., Hellstrom, J., Paul, B., Woodhead, J., Hergt, J., 2011. Iolite: freeware for the visualisation and processing of mass spectrometric data. J. Anal. At. Spectrom 26 (12), 2508. https://doi.org/10.1039/c1ja10172b.
Qi, Y.Q., Hu, R.Z., Gao, J.F., Leng, C.B., Gao, W., Gong, H.T., 2022. Trace and minor elements in sulfides from the Lengshuikeng Ag-Pb-Zn deposit, South China: a LA-ICP-MS study. Ore Geol. Rev. 141, 104663 https://doi.org/10.1016/j.oregeorev.2021.104663.
Reich, M., Deditius, A., Chryssoulis, S., Li, J.W., Ma, C.Q., Parada, M.A., Barra, F., Mittermayr, F., 2013. Pyrite as a record of hydrothermal fluid evolution in a porphyry copper system: a SIMS/EMPA trace element study. Geochim. Cosmochim. Ac. 104, 42–62. https://doi.org/10.1016/j.gca.2012.11.006.
Roberts, N.M.W., Rasbury, E.T., Parrish, R.R., Smith, C.J., Horstwood, M.S.A., Condon, D.J., 2017. A calcite reference material for LA-ICP-MS U-Pb geochronology. Geochem. Geophys. Geosyst. 18 (7), 2807–2814. https://doi.org/10.1002/2016GC006784.
Román, N., Reich, M., Leisen, M., Morata, D., Barra, F., Deditius, A.P., 2019. Geochemical and micro-textural fingerprints of boiling in pyrite. Geochim. Cosmochim. Ac. 246, 60–85. https://doi.org/10.1016/j.gca.2018.11.034.
Sack, R.O., Lynch, J.V.G., Foit, F., 2003. Fahlore as a petrogenetic indicator: Keno Hill Ag-Pb-Zn District, Yukon, Canada. Mineral. Mag. 67 (5), 1023–1038. https://doi.org/10.1180/0026461036750141.
Seal, R.R., 2006. Sulfur isotope geochemistry of sulfide minerals. Rev. Mineral. Geochem. 61 (1), 633–677. https://doi.org/10.2138/rmg.2006.61.12.
Selby, D., Creaser, R.A., Hart, C.J.R., Rombach, C.S., Thompson, J.F.H., Smit, M.T., Bakke, A.A., Goldfarb, R.J., 2002. Absolute timing of sulfide and gold mineralization: a comparison of Re-Os molybdenite and Ar-Ar mica methods from the Tintina Gold Belt, Alaska. Geology 9 (30), 791–794. https://doi.org/10.1130/0091-7613.
Wang, L., Tang, L., Zhang, S.T., Santosh, M., Song, K.R., Sheng, Y.M., Feng, J.Y., 2022. Genesis of a Ag-Pb-Zn-F system: Insights from in situ sulfur isotope and trace elements of pyrite, and rare earth elements of fluorite in the Baiyine'lebu deposit, Inner Mongolia, China. Ore Geol. Rev. 141, 104667 https://doi.org/10.1016/j.oregeorev.2021.104667.
Wei, D.T., Xia, Y., Gregory, D.D., Steadman, J.A., Tan, Q.P., Xie, Z.J., Liu, X.J., 2020. Multistage pyrites in the Nibao disseminated gold deposit, southwestern Guizhou Province, China: insights into the origin of Au from textures, in situ trace elements, and sulfur isotope analyses. Ore Geol. Rev. 122, 103446 https://doi.org/10.1016/j.oregeorev.2020.103446.
Woodhead, J.D., Hergt, J.M., Carignan, J., Telouk, P., Valladon, M., 2001. Strontium, neodymium and lead isotope analyses of NIST glass certified reference materials; SRM 610, 612, 614. Geostand. Newslett. 25 (2–3), 261–266. https://doi.org/10.1111/j.1751-908X.2001.tb00601.x.
Wu, Y.F., 2019. Geological characteristics and genesis of the Nagengkangqiergou silver deposit in Dulan County, Qinghai Province. In: Chinese with English Abstract. Jilin University, p. 57 (Master Thesis).
Wu, J.J., Zeng, Q.D., Santosh, M., Fan, H.R., Wei, Z.H., Yang, K.F., Zhang, Z.M., Li, X.H., Liang, G.Z., 2021. Intrusion-related orogenic gold deposit in the East Kunlun belt, NW China: a multiproxy investigation. Ore Geol. Rev. 139, 104550 https://doi.org/10.1016/j.oregeorev.2021.104550.
Xu, Z.Q., Li, H.B., Yang, J.S., 2006. An orogenic plateau—the orogenic collage and orogenic types of the Qinghai-Tibet plateau. Earth Sci. Front. 13(04), 1–17 (in Chinese with English abstract).
Xu, C.W., Wei, J.H., Zhou, H.Z., Zhao, X., Zhang, S.T., Li, W.J., 2020. S-Pb isotope characteristics and prospecting model of the Nagengkangqieer silver deposit in the eastern segment of East Kunlun Mountain. Geol. Bull. China 39 (05), 712–727 (in Chinese with English abstract).
Yan, X., Chen, B., Duan, X.X., Wang, Z.Q., 2021. Geochronology and ore genesis of the Niujuan-Yingfang Pb-Zn-Ag deposit in Fengning, Northern North China Craton: constraints from fluid inclusions, H-O-S isotopes and fluorite Sr-Nd isotopes. J Earth Sci. China 32 (1), 81–102. https://doi.org/10.1007/s12583-020-1393-8.
Ye, L., Cook, N.J., Ciobanu, C.L., Liu, Y., Zhang, Q., Liu, T., Gao, W., Yang, Y., Danyushevskiy, L., 2011. Trace and minor elements in sphalerite from base metal deposits in South China: a LA-ICPMS study. Ore Geol. Rev. 39 (4), 188–217. https://doi.org/10.1016/j.oregeorev.2011.03.001.
Yu, M., Feng, C.Y., Santosh, M., Mao, J.W., Zhu, Y.F., Zhao, Y.M., Li, D.X., Li, B., 2017. The Qiman Tagh Orogen as a window to the crustal evolution in northern Qinghai-Tibet Plateau. Earth Sci. Rev. 167, 103–123. https://doi.org/10.1016/j.earscirev.2017.02.008.
Yu, M., Dick, J.M., Feng, C.Y., Li, B., Wang, H., 2020b. The tectonic evolution of the East Kunlun Orogen, northern Tibetan Plateau: a critical review with an integrated geodynamic model. J. Asian Earth Sci. 191, 104168 https://doi.org/10.1016/j.jseaes.2019.104168.
Yu, D.S., Xu, D.R., Zhao, Z.X., Huang, Q.Y., Wang, Z.L., Deng, T., Zou, S.H., 2020a. Genesis of the Taolin Pb-Zn deposit in northeastern Hunan Province, South China: constraints from trace elements and oxygen-sulfur-lead isotopes of the hydrothermal minerals. Miner. Deposita 55 (7), 1467–1488. https://doi.org/10.1007/s00126-019-00947-8.
Yuan, C., Zhou, M.F., Sun, M., Zhao, Y.J., Wilde, S., Long, X.P., Yan, D.P., 2010. Triassic granitoids in the eastern Songpan Ganzi Fold Belt, SW China: magmatic response to geodynamics of the deep lithosphere. Earth Planet Sc. Lett. 290 (3–4), 481–492. https://doi.org/10.1016/j.epsl.2010.01.005.
Zhai, Y.S., Deng, J., Cui, B., Ding, W.J., Peng, R.M., Wang, J.P., Yang, L.Q., 1999. Ore-forming system and comprehensive geo-anomaly. Geoscience 13(1), 99–104 (in Chinese with English abstract).
Zhai, D.G., Liu, J.J., Cook, N.J., Wang, X.L., Yang, Y.Q., Zhang, A.L., Jiao, Y.C., 2019. Mineralogical, textural, sulfur and lead isotope constraints on the origin of Ag-Pb-Zn mineralization at Bianjiadayuan, Inner Mongolia, NE China. Miner. Deposita 54 (1), 47–66. https://doi.org/10.1007/s00126-018-0804-6.
Zhai, D.G., Williams-Jones, A.E., Liu, J.J., Selby, D., Voudouris, P.C., Tombros, S., Li, K., Li, P.L., Sun, H.J., 2020. The genesis of the giant shuangjianzishan epithermal Ag-Pb-Zn deposit, Inner Mongolia, Northeastern China. Econ. Geol. 115 (1), 101–128. https://doi.org/10.5382/econgeo.4695.
Zhang, X.M., Li, Y.J., Zhang, S.T., Li, W.W., Xu, C.W., Kamradt, A., Borg, G., Wei, J.H., 2023a. Geochronology, pyrite trace elements, and in-situ S isotopes of the giant Nagengkangqie'er silver deposit in the Eastern Kunlun Orogenic Belt, Northern Tibetan Plateau. Ore Geol. Rev. 162, 105696 https://doi.org/10.1016/j.oregeorev.2023.105696.
Zhang, J.Y., Ma, C.Q., Xiong, F.H., Liu, B., Li, J.W., Pan, Y.M., 2014. Early Paleozoic High-Mg diorite-granodiorite in the eastern Kunlun Orogen, western China: response to continental collision and slab break-off. Lithos 210–211, 129–146. https://doi.org/10.1016/j.lithos.2014.10.003.
Zhang, J.Y., Ma, C.Q., Li, J.W., Pan, Y.M., 2017. A possible genetic relationship between orogenic gold mineralization and post-collisional magmatism in the eastern Kunlun Orogen, western China. Ore Geol. Rev. 81, 342–357. https://doi.org/10.1016/j.oregeorev.2016.11.003.
Zhang, P.C., Peng, B., Zhao, J., Guo, G.F., Zuo, Y.S., Xing, Y.Q., 2022. Genesis of the Bayan qagan dongshan Sn-Pb-Zn-Ag deposit, NE China, based on sphalerite chemistry and sulfur isotope. Ore Geol. Rev. 150, 105124 https://doi.org/10.1016/j.oregeorev.2022.105124.
Zhang, B., Yang, T., Yang, S.F., Li, J.C., Kong, H.L., 2018. The metallic minerals and S and Pb Isotope compositions of the Harizha Lead-Zinc polymetallic deposit, East Kunlun. Geoscience 32 (04), 646–654 (in Chinese with English abstract).
Zhang, X.M., Zhao, X., Fu, L.B., Li, Y.J., Kamradt, A., Santosh, M., Xu, C.W., Huang, X.K., Borg, G., Wei, J.H., 2023b. Crustal architecture and metallogeny associated with the Paleo-Tethys evolution in the Eastern Kunlun Orogenic Belt, Northern Tibetan Plateau. Geosci. Front. 14 (6), 101654 https://doi.org/10.1016/j.gsf.2023.101654.
Zhao, X., 2020. Tectono-magmatic transformation and gold mineralization in the Gouli area, the East Kunlun orogen. In: Chinese with English Abstract. China University of Geosciences, p. 176 (Ph.D. thesis).
Zhao, H.X., Frimmel, H.E., Jiang, S.Y., Dai, B.Z., 2011. LA-ICP-MS trace element analysis of pyrite from the Xiaoqinling gold district, China: implications for ore genesis. Ore Geol. Rev. 43 (1), 142–153. https://doi.org/10.1016/j.oregeorev.2011.07.006.
Zhao, X., Fu, L.B., Wei, J.H., Huizenga, J.M., Liu, Y., Chen, J.J., Wang, D.Z., 2021. Generation and structural modification of the giant Kengdenongshe VMS-type Au-Ag-Pb-Zn polymetallic deposit in the East Kunlun Orogen, East Tethys: constraints from geology, fluid inclusions, noble gas and stable isotopes. Ore Geol. Rev. 131, 104041 https://doi.org/10.1016/j.oregeorev.2021.104041.
Zhao, X., Fu, L., Santosh, M., Wei, J., Chen, J., 2022a. The growth and evolution of continental crust contributed by multiple sources in the East Kunlun Orogen during Early Paleozoic. Earth Sci. Rev. 233, 104190 https://doi.org/10.1016/j.earscirev.2022.104190.
Zhao, X., Fu, L.B., Santosh, M., Wei, J.H., Zhang, C., Chen, J.J., Xu, C.W., Zhang, X.M., 2022b. Petrogenesis of the Triassic andesites in the East Kunlun Orogen, East Tethys: implications for crustal maturation within an extensional setting. J. Geol. Soc. London 180. https://doi.org/10.1144/jgs2022-124.
Zhong, S.H., Feng, C.Y., Seltmann, R., Li, D.X., 2017. Middle Devonian volcanic rocks in the Weibao Cu–Pb–Zn deposit, East Kunlun Mountains, NW China: zircon chronology and tectonic implications. Ore Geol. Rev. 84, 309–327. https://doi.org/10.1016/j.oregeorev.2017.01.020.
Zhong, S., Feng, C., Seltmann, R., Dolgopolova, A., Andersen, J.C.Ø., Li, D., Yu, M., 2018. Sources of fluids and metals and evolution models of skarn deposits in the Qimantagh metallogenic belt: a case study from the Weibao deposit, East Kunlun Mountains, northern Tibetan Plateau. Ore Geol. Rev. 93, 19–37. https://doi.org/10.1016/j.oregeorev.2017.12.013.
Zong, K.Q., Klemd, R., Yuan, Y., He, Z.Y., Guo, J.L., Shi, X.L., Liu, Y.S., Hu, Z.C., Zhang, Z.M., 2017. The assembly of Rodinia: The correlation of early Neoproterozoic (ca. 900 Ma) high-grade metamorphism and continental arc formation in the southern Beishan Orogen, southern Central Asian Orogenic Belt (CAOB). Precambr. Res. 290, 32–48. https://doi.org/10.1016/j.precamres.2016.12.010.